



NKS-283  
ISBN 978-87-7893-358-4

---

# Modelling of pressure loads in a pressure suppression pool

Antti Timperi  
Michael Chauhan  
Timo Pättikangas  
Jarto Niemi

VTT Technical Research Centre of Finland

April 2013

## Abstract

Rapid collapse of a large steam bubble is analyzed by using CFD and FEM calculations. In addition, a 1D code is written which takes into account the finite condensation rate. The 1D simulations are compared with the PPOOLEX experiment COL-01. By adjusting the condensation rate, the calculated pressure peak near the vent outlet could be made same as in the experiment. Scaling of the measured pressure loads to full-scale is studied by dimensional analyses and by review of the analysis of Sonin (1981).

The structural response of containment during chugging is studied by using an FEM of containment with simplified geometry and loading which was created based on experimental data. The results are compared to the case in which desynchronization is absent, and chugging occurs simultaneously in every vent pipe. The desynchronized loading is created by giving random initiation times for chugs out of distribution corresponding to the desynchronization time presented by Kukita and Namatame (1985).

CFD simulations of the PPOOLEX experiment MIX-03 were performed. In the experiment, clear chugging behavior was observed. In the simulation, the interphasial surface was much more stable and oscillation occurred at a higher frequency than in the experiment. The differences are likely caused by the turbulence model and too coarse numerical mesh, which causes numerical diffusion.

## Key words

Condensation pool, pressure suppression pool, BWR, CFD, fluid-structure interaction, FSI, chugging, LOCA

NKS-283  
ISBN 978-87-7893-358-4

Electronic report, June 2013

NKS Secretariat  
P.O. Box 49  
DK - 4000 Roskilde, Denmark

Phone +45 4677 4041  
www.nks.org  
e-mail nks@nks.org






# Modelling of pressure loads in a pressure suppression pool

Authors: Antti Timperi, Michael Chauhan, Timo Pättikangas, and Jarto Niemi

Confidentiality: Public



<b>Report's title</b>	
Modelling of pressure loads in a pressure suppression pool	
<b>Customer, contact person, address</b>	<b>Order reference</b>
1. Valtion ydinjäterahasto, Työ- ja elinkeinoministeriö, PL 32, 00023 VALTIONEUVOSTO 2. Nordic nuclear safety research (NKS), c/o Fortum Power and Heat Oy, Kaisu Leino, PL 100, 00048 FORTUM	1. SAFIR2014 Programme: Dnro 25/2012SAF 2. NKS Contract no. AFT/NKS-R(12)90/6
<b>Project name</b>	<b>Project number/Short name</b>
Numerical modelling of condensation pool	73955 / NUMPOOL2012
<b>Author(s)</b>	<b>Pages</b>
Antti Timperi, Michael Chauhan, Timo Pättikangas, and Jarto Niemi	55
<b>Keywords</b>	<b>Report identification code</b>
Condensation pool, pressure suppression pool, BWR, CFD, fluid-structure interaction, FSI, chugging, LOCA	VTT-R-01563-13
<b>Summary</b>	
<p>Rapid collapse of a large steam bubble is analyzed by using CFD and FEM calculations. In addition, a 1D code is written which takes into account the finite condensation rate. The 1D simulations are compared with the PPOOLEX experiment COL-01. By adjusting the condensation rate, the calculated pressure peak near the vent outlet could be made same as in the experiment. Scaling of the measured pressure loads to full-scale is studied by dimensional analyses and by review of the analysis of Sonin (1981) on SRV discharge.</p> <p>The structural response of containment during chugging is studied by using a finite element model of containment with simplified geometry and loading which was created based on experimental data. The results are compared to a case in which desynchronization is absent, and chugging occurs simultaneous in every vent pipe. The desynchronized loading is created by giving random initiation times for chugs out of distribution corresponding to the desynchronization time presented by Kukita and Namatame (1985).</p> <p>CFD simulations of the PPOOLEX experiment MIX-03 were performed. In the experiment, clear chugging behavior was observed. In the simulation, the interphasial surface was much more stable and oscillation occurred at a higher frequency than in the experiment. The differences are likely caused by the turbulence model and too coarse numerical mesh, which causes numerical diffusion.</p>	
<b>Confidentiality</b>	Public
Espoo, 28 February, 2013	
<b>Written by</b>	<b>Reviewed by</b>
 Timo Pättikangas, Principal Scientist	 Mikko Manninen, Team Leader
	<b>Accepted by</b>
	 Timo Vanttola, Technology Manager
<b>VTT's contact address</b>	
VTT Technical Research Centre of Finland, P.O.B. 1000, FI-02044 VTT, Finland	
<b>Distribution (customer and VTT)</b>	
Kaisu Leino (NKS), STUK, Timo Toppila (Fortum), Vesa Suolanen (VTT), Pavel Kudinov (KTH), Vesa Tanskanen (LUT), Markku Puustinen (LUT), Heikki Purhonen (LUT), Jani Laine (LUT), SAFIR2014 Reference Group 4	
<p><i>The use of the name of the VTT Technical Research Centre of Finland (VTT) in advertising or publication in part of this report is only permissible with written authorisation from the VTT Technical Research Centre of Finland.</i></p>	

## Preface

---

This work has been carried out in the NUMPOOL project of the SAFIR2014 programme (The Finnish Research Programme on Nuclear Power Plant Safety). The project has been funded by Valtion ydinjäterahasto, VTT and NKS (Nordic nuclear safety research). The authors are grateful for comments obtained from the members of the SAFIR2010 Reference Group 4 and from the Northnet Roadmap 3 Reference Group.

Espoo 28.2.2013

Authors

## Contents

---

Preface.....	2
Contents.....	3
1. Introduction.....	4
2. Calculation of the bubble collapse.....	6
3. Scaling of the experimental pressure loads to BWR.....	12
3.1 Sonin (1981) analysis .....	12
3.2 Pressure loss in a pipe.....	15
3.3 Vent clearing transient .....	16
3.4 Bubble rise in the pool .....	17
3.5 Condensation water hammer .....	18
3.6 Single-phase mass and energy flow scaling .....	20
4. Description of the numerical model for a BWR containment.....	23
4.1 Simplified model .....	23
4.2 Analysis type .....	26
4.3 Analysis comparison.....	27
5. Desynchronization characteristics.....	29
6. Description of the loading.....	30
7. Results and discussion .....	32
7.1 Structural response during chugging.....	32
8. CFD modeling of PPOOLEX experiment MIX-03 .....	40
8.1 PPOOLEX experiment MIX-03.....	40
8.2 Numerical model.....	40
8.3 Results of CFD simulations.....	41
9. Summary and conclusions .....	46
References.....	48

## 1. Introduction

---

In boiling water reactors (BWRs), the major function of the containment system is to protect the environment if a loss-of-coolant accident (LOCA) should occur. The containment is designed to accommodate the loads generated in hypothetical accidents, such as sudden rupture of a main steam line. In such an accident, a large amount of steam is suddenly released in the containment. An essential part of the pressure suppression containment is a water pool, where condensation of released steam occurs.

In a BWR, the pressure suppression containment typically consists of a drywell and a wetwell with a water pool. In the hypothetical LOCA, steam and air flow from the drywell through vent pipes to the wetwell, where the outlets of the vent pipes are submerged in the water pool. In the early part of the accident, mainly non-condensable air or nitrogen flows through the vent pipes into the wetwell. Then, the volume fraction of vapor increases in the gas mixture. When all the non-condensable gas from the drywell has been blown into the wetwell, the blowdown consists of pure vapor. At this stage, so-called chugging effect may occur, which means periodic formation and rapid condensation of large vapor bubbles at the vent outlets (Lahey and Moody, 1993). The rapid condensation of the vapor bubbles may induce significant pressure loads on the structures in the pressure suppression pool and on the containment.

One of the main concerns during the LOCA is the pressure loads caused by the rapid condensation of large steam bubbles. The collapses of the bubbles occur usually during the chugging phase of the discharge, when pure or nearly pure steam is injected into the pool with a relatively low flow rate. In the earlier work, 1D and 2D calculations of collapses of spherical and toroidal bubbles were performed analytically and numerically (Pättikangas et al., 2011; Timperi et al., 2012). It was shown by Timperi et al. (2012) that the pressure load amplitude and pulse width as well as the collapse time are all quite similar for spherical and toroidal bubbles having same volumes. Collapses of spherical and toroidal bubbles were compared for different bubble sizes, pressure differences, bubble initial pressures and water sonic velocities. When comparing the calculated and measured pressure loads, however, there were significant differences. The calculated pressure peaks were much too high and narrow compared to the experiments, the difference being approximately an order of magnitude for both the amplitude and pulse width. There are several possible reasons for this, one being that an instantaneous steam condensation was assumed in the calculations. In the present work, we attempt to refine the calculations by taking into account the finite condensation rate. This is difficult to accomplish in the 2D Eulerian calculations of toroidal bubbles performed earlier and, therefore, 1D calculations assuming spherical symmetry are performed. However, this assumption can be justified based on the earlier work as discussed above.

Scaling of the pressure loads from the laboratory experiments to full-scale BWR containment is another important topic. The scaling is studied in this work by dimensional analysis and by review of the work by Sonin (1981) on nearly the same subject. The main assumptions, consequences and unaddressed issues in the Sonin (1981) analysis are first discussed. Dimensional analyses are then performed separately for different phenomenon during the LOCA: pressure loss in a pipe, initial vent clearing transient, bubble rise in the pool, collapse of the vapor bubble as well as mass and energy flow scaling.

Earlier studies on chugging (see Kukita and Namatame, 1985 and Puustinen et. al. 2011) suggest that the chug events occurs slightly asynchronously between different pipes, which in turn affect the magnitude of the pool boundary loads. In this study, the effect of desynchronization of chug events to the structural response is studied and compared against a case in which chugging occurs simultaneously in all pipes. The asynchronous loading is formed using test data from large scale tests and chugging is simulated in a simplified model



of BWR containment. Due to the dynamic nature of the phenomenon, and large structure, the computation is time consuming and result files become excessively large in size. The simplified model geometry enables the computation of multiple chug events, during which the desynchronization time varies from pipe to pipe. This way, the structural response can be studied more realistically. The aim of this study is to develop a method for modeling the chugging phenomena realistically, rather than computing the absolute stress or displacement values.

Experiments performed at the Lappeenranta University of Technology with the PPOOLEX facility are modeled with Computational Fluid Dynamics (CFD) calculations. PPOOLEX is a pressurized facility consisting of a drywell compartment and a wetwell compartment with a water pool (Puustinen et al., 2011). In experiments, steam flows through a vent pipe from the drywell to the water pool in the wetwell. Direct contact condensation in the chugging phase of the experiments is modeled with CFD calculations.

In Sec. 2, the collapse of a single vapor bubble is first studied by using a simplified numerical model which is compared to experimental results obtained with the PPOOLEX facility. The scaling of the loads obtained with experimental facilities to full size BWR containments is discussed in Sec. 3. A Finite Element Method (FEM) model for a BWR containment with 16 vent pipes is described in Sec. 4. The desynchronization effects between the vent pipes are discussed in Sec. 5, and the construction of loading from the available data is described in Sec. 6. The results of the FEM calculations are presented in Sec. 7. CFD calculations of direct contact condensation are described in Sec. 8. Finally, the results are summarized in Sec. 9.

## 2. Calculation of the bubble collapse

A Fortran program was written, which solves the one-dimensional dynamics of a spherical, collapsing steam bubble and where the finite steam condensation rate can be accounted for.

The starting point is a spherical bubble in infinite incompressible fluid. The assumption of incompressible fluid is justified here for examining the collapse based on the fairly low and wide pressure peaks observed in the experiments, although away from the bubble compressibility has an effect since the pressure peak propagates as a sound wave. Using potential flow formulation, the so-called Rayleigh equation for the bubble radius can be derived (Moody, 1990):

$$R \frac{d^2 R}{dt^2} + \frac{3}{2} \left( \frac{dR}{dt} \right)^2 = \frac{1}{\rho} (p_B(t) - p_\infty) \quad (1)$$

where  $R$  is the bubble radius,  $t$  is time,  $\rho$  is fluid density,  $p_B$  is pressure inside the bubble and  $p_\infty$  is pressure far away from the bubble. Solution of this equation for an arbitrary bubble pressure was implemented as a Fortran code. The first time-derivative is approximated as

$$\frac{dR}{dt} \approx \frac{R_n - R_{n-1}}{\Delta t} \quad (2)$$

where the index  $n$  stands for the discrete time instants and  $\Delta t$  is the time step. Similarly, the second time-derivative is approximated as

$$\frac{d^2 R}{dt^2} \approx \frac{R_{n+1} - 2R_n + R_{n-1}}{\Delta t^2} \quad (3)$$

Inserting the time-derivatives into Eq. (1), we obtain

$$R_n \frac{R_{n+1} - 2R_n + R_{n-1}}{\Delta t^2} + \frac{3}{2} \left( \frac{R_n - R_{n-1}}{\Delta t} \right)^2 = \frac{1}{\rho} (p_B(t) - p_\infty) \quad (4)$$

Thus, an explicit solution for  $R$  for the next time  $n + 1$  is obtained as

$$R_{n+1} = \frac{\Delta t^2}{\rho R_n} (p_B(t) - p_\infty) - \frac{3}{2} \frac{(R_n - R_{n-1})^2}{R_n} + 2R_n - R_{n-1} \quad (5)$$

Here we assume the ideal gas law for steam inside the bubble. The steam is assumed to be saturated at all times, and hence the steam temperature is obtained from the pressure according to the saturation line. Steam mass in the bubble is calculated from either

$$m(t) = m_0 - \int_0^t c dt \quad (6)$$

or

$$m(t) = m_0 - \int_0^t c'' A(t) dt \quad (7)$$

where  $t$  is time,  $m_0$  is the steam initial mass (calculated from the initial pressure and temperature according to the ideal gas law),  $c$  and  $c''$  are the condensation rates (constants in this work) and  $A$  is the bubble surface area. In the first case, the total condensation rate is constant, while in the second case condensation rate per bubble surface area is constant.

The code was first validated against earlier analytical and numerical solutions for the case of infinite condensation rate, i.e. instantaneous condensation of steam in the bubble (Pättikangas et al., 2011). Figure 1 shows bubble radius, surface velocity and surface acceleration for the simplified case of constant pressure difference  $\Delta p = p_\infty - p_{B,0}$ . Here we have used values  $\Delta p = 1$  bar,  $\rho = 1000$  kg/m<sup>3</sup>,  $R_0 = 1$  m and  $\Delta t = 10^{-5}$  s. It is seen that all quantities agree very well with the analytical solution. Figure 2 shows corresponding results for the case where there is some amount of air left in the bubble, using values  $p_{B,0} = 0.05$  bar,  $T_{B,0} = 293$  K,  $p_\infty = 1$  bar,  $\rho = 1000$  kg/m<sup>3</sup>,  $R_0 = 1$  m and  $\Delta t = 10^{-4}$  s. Also in this case the 1D code and the analytical solution agree well with each other, while there are some differences compared to the Abaqus solution, as discussed briefly by Pättikangas et al., 2011.

In modeling with finite condensation rate, the PPOOLEX experiment COL-01 was considered. This experiment was analyzed already in the previous work by Timperi et al. (2012). Four bubble collapses giving the largest pressure loads were searched from the experimental data and the maximum sizes of the toroidal bubbles right before the collapses were determined from the high-speed video recordings. The small bubble sizes and large pressure loads indicated large condensation rate of steam in the bubble.

In the experiment COL-01 during the chugging phase, the state of steam was only slightly above the saturation line (only slightly superheated), since the steam pressure and temperature measured at the vent pipe outlet were about 2.8 bar and 132 °C, respectively (Laine et al., 2009). Thus, in the modeling we set the steam and water initial pressure to 2.8 bar, from which it results according to the saturation line that the steam initial temperature is set to 131.4 °C. The bubble initial radius is set so that same initial volume results as for the toroidal bubbles observed in the experiment, i.e.  $R_0 = 83$  mm (Timperi et al., 2012). Time step in the modeling was set to  $\Delta t = 10^{-5}$  s.

From the analytical solution, the bubble collapse time for constant pressure difference is (Pättikangas et al., 2011)

$$t_{coll} = 0.915 R_0 \sqrt{\frac{\rho}{\Delta p}} \quad (8)$$

For the used initial conditions and assuming instantaneous and complete steam condensation, i.e.  $\Delta p = 2.8$  bar, we obtain from Eq. (8)  $t_{coll} \approx 4.54$  ms. This is shorter than the experimental collapse times of 7...10 ms in the COL-01 experiment.

The initial steam mass with the used initial conditions is  $m_0 \approx 3.6$  g. Assuming collapse times in the range of 7...10 ms results then in average condensation rate in the range of 360...514 g/s. For comparison, the steam flow rate into the drywell was about 435 g/s in the COL-01 experiment (Laine et al., 2009). However, in comparing the condensation rate in the bubble during the collapse to the steam flow rate into the drywell, one must remember that i) part of the steam condenses at the steel walls of the drywell and at the vent pipe inner wall and ii) the bubble collapse time is very short compared to the growth time of the bubble, during which condensation also occurs.

In Figure 3, the modeled results of the bubble collapse are plotted as functions of time when i) the total condensation rate is constant and ii) the condensation rate per bubble surface area is constant. In Figure 4, the pressure loads near the vent pipe outlet are compared with the experiment for cases where the condensation rate has been adjusted to give approximately correct peak pressure. For the calculations, pressure is presented 200 mm from the bubble centre, where the pressure amplitude was found about the same as for the toroidal bubbles at the location of the P5 sensor (Timperi et al., 2012).

When the condensation rate is low, there is still steam left in the bubble at the moment of peak volume acceleration, which restricts the decrease of the bubble radius and thus dampens the pressure loads effectively. When the condensation rate is high, there is little or no steam in the bubble at the final phase of the collapse, resulting in very high peak pressures. When the peak pressure is about the same as in the experiments, the bubble surface velocity stays quite moderate, i.e. well below the sonic velocity in water, which would indicate that the assumption of incompressible water is justified in these cases. When the peak pressure is correct, the collapse times are somewhat longer in the calculations.

It is noteworthy that the results are sensitive to the condensation rate, i.e. small changes in the condensation rate lead to large changes in the peak pressure. This is because the peak volume acceleration is sensitive to the amount of steam in the bubble at the final phase. When there still is steam in the bubble at the moment of peak volume acceleration, the steam pressure rise slows down the bubble surface velocity at the important final phase. This sensitivity makes the simulation results questionable.

From Figure 4 one also notes that during the low-pressure phase of the collapse, the experimental pressures show larger pressure drop than the calculated ones. In the calculations, the pressure drop can be made larger and the collapse time shorter by increasing the condensation rate, but this increases the peak pressures significantly.

In the above calculations, no non-condensable gas was assumed in the bubble. A significant amount of non-condensable gas left after the condensed steam could lower and broaden the pressure peaks, but the experiments (Puustinen, 2006) as well as the present and earlier (Timperi et al., 2012) calculations indicate that the largest possible amount of non-condensable gas that can in reality exist during the large peak pressures in the chugging is too small to cause such a large difference. In the experiments by Puustinen (2006), the peak loads were still visible but air had an effect on them with air mass fractions of about 1 %, while at air mass fractions of 3 %, the damping of the water hammer loads was already practically complete.

There are several possible reasons for the much lower and wider experimental pressure peaks compared to the calculations:

- In the calculations, the condensation rate (either total or per surface area) was constant, but in reality the condensation rate may be large initially and slow down significantly, resulting in incomplete condensation in the final phase.
- The high-speed videos show that the bubble shapes are fairly irregular (see Timperi et al., 2012). Condensation may take place slightly “asynchronously” in different parts of the toroidal bubble.
- In the final phase, the bubble shape may become highly irregular and/or the bubble surface may break into a “soft” two-phase mixture.

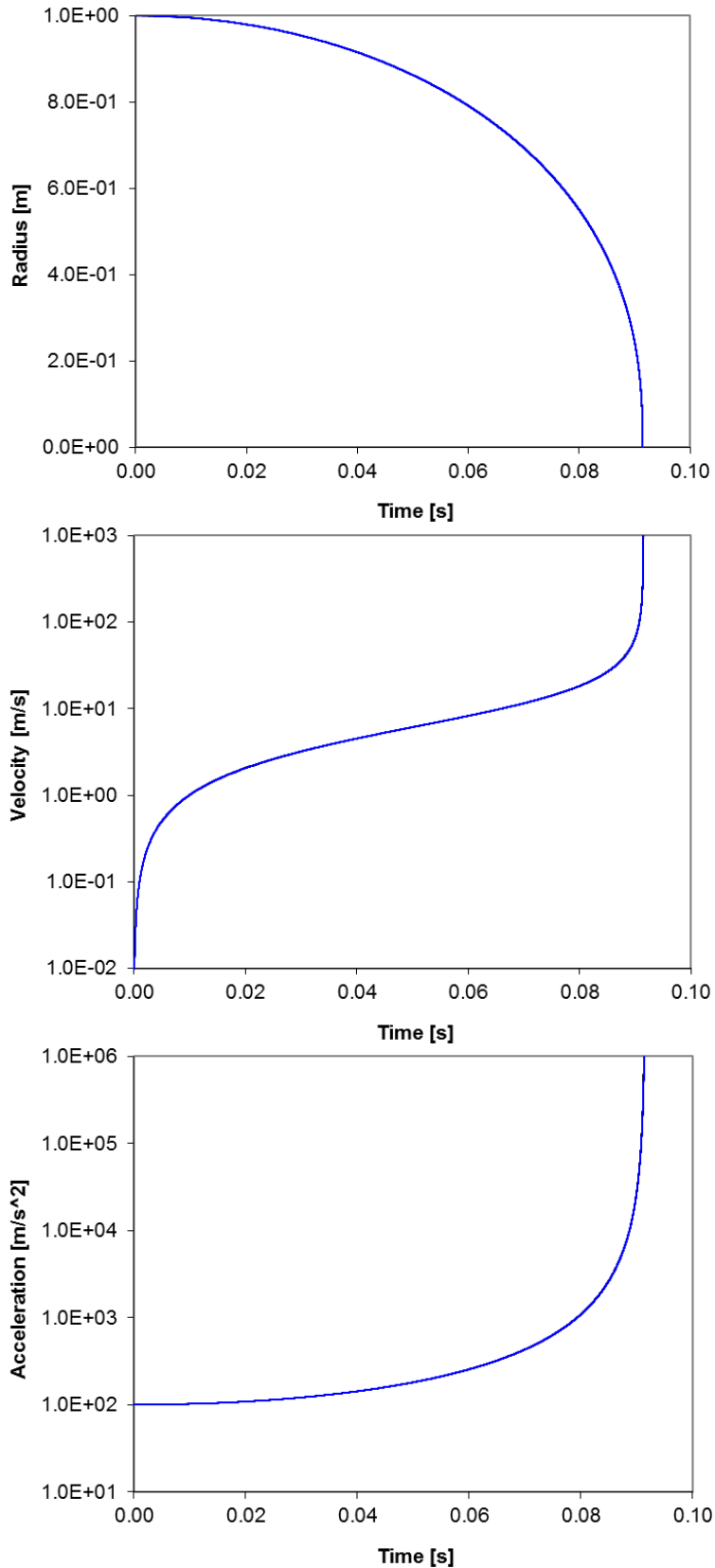


Figure 1. Bubble radius, surface velocity and surface acceleration with constant bubble pressure. Difference between the ambient and bubble pressure is 1 bar. (— 1D code, — Analytical)

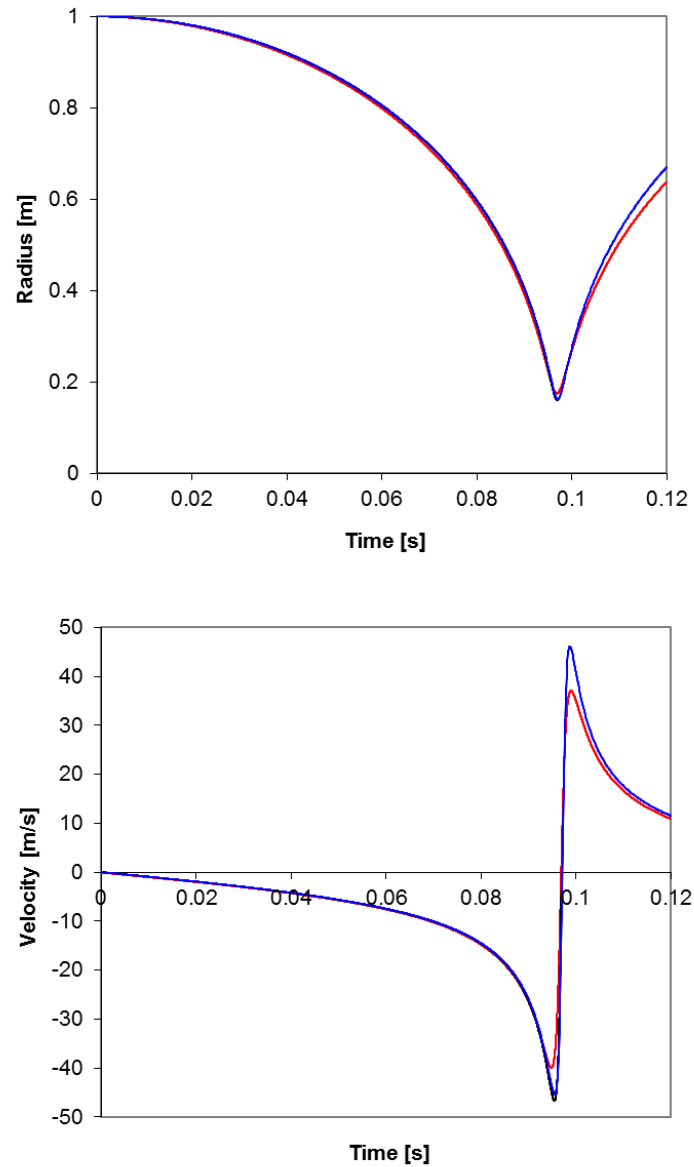


Figure 2. Bubble radius and surface velocity for a non-condensable ideal gas bubble. The initial bubble pressure is 0.05 bar and the ambient pressure is 1 bar. (— 1D code, — Abaqus, — Analytical)

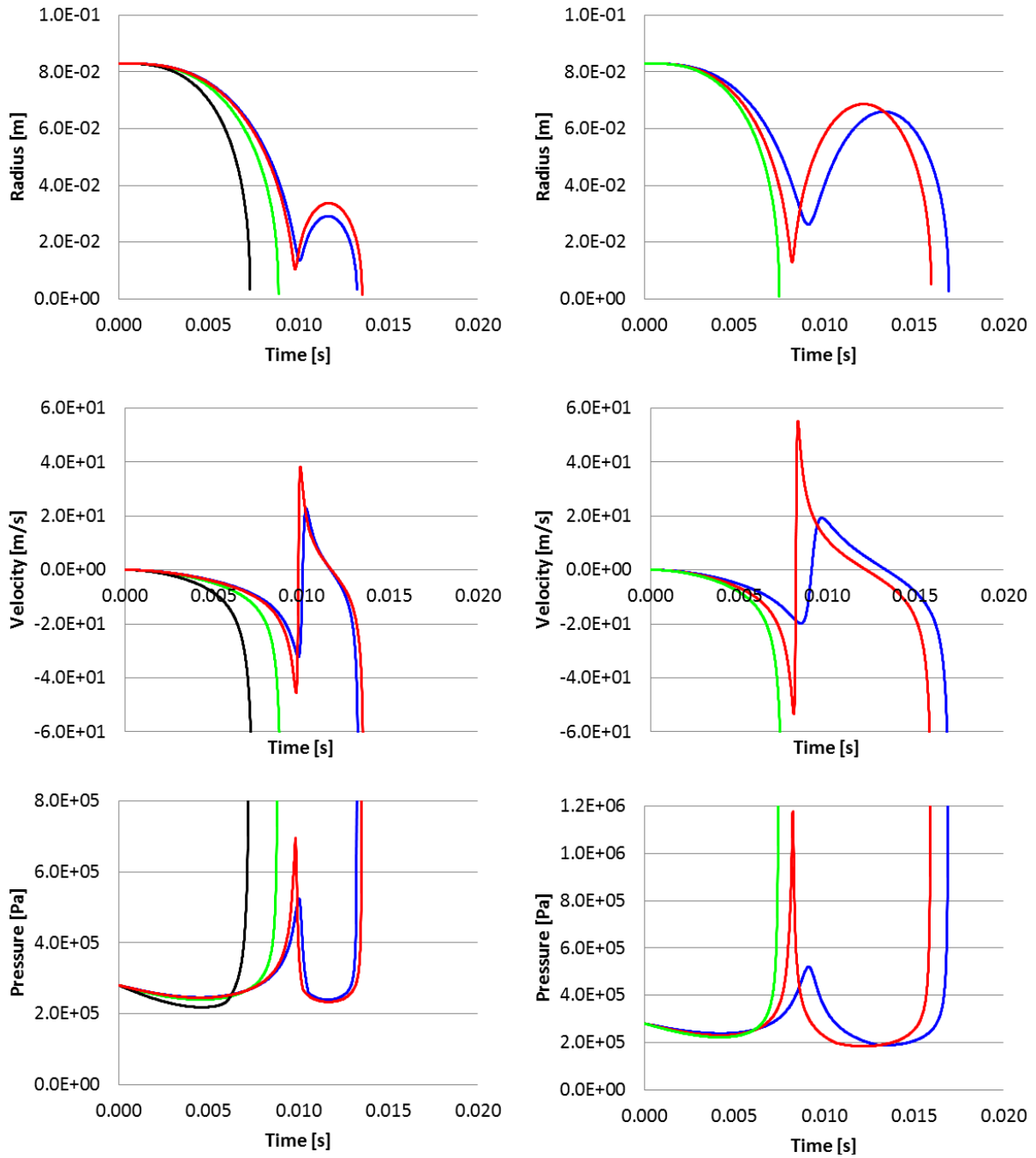


Figure 3. Calculated bubble radius, surface velocity and pressure 200 mm from bubble center in PPOOLEX experiment COL-01. On the left: total condensation rate ( $c = 0.34$  kg/s,  $c = 0.35$  kg/s,  $c = 0.4$  kg/s,  $c = 0.6$  kg/s); on the right: condensation rate per surface area ( $c'' = 5$  kg/m<sup>2</sup>s,  $c'' = 6$  kg/m<sup>2</sup>s,  $c'' = 7$  kg/m<sup>2</sup>s).

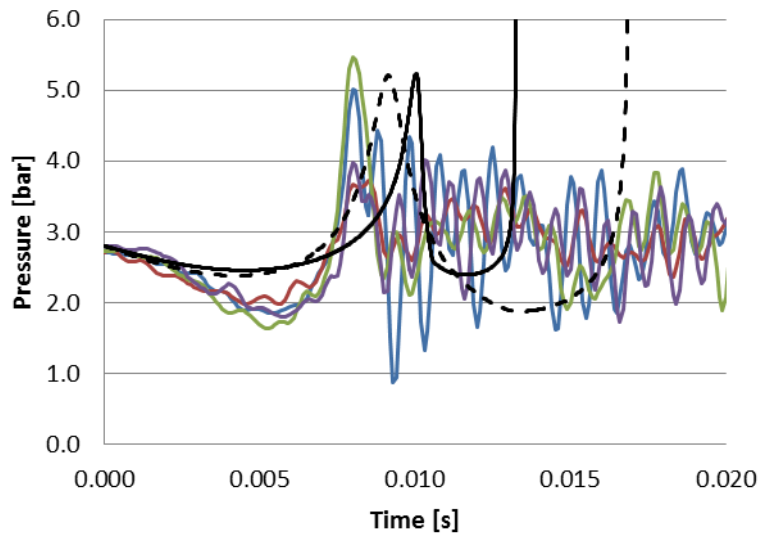


Figure 4. Measured (sensor P5) and calculated (200 mm from bubble center) pressures in PPOOLEX experiment COL-01. (— Bubble 1, — Bubble 2, — Bubble 3, — Bubble 4, — Total condensation rate  $c = 0.34$  kg/s, --- Condensation rate per surface area  $c'' = 5$  kg/m<sup>2</sup>s)

### 3. Scaling of the experimental pressure loads to BWR

Scaling of the pressure loads measured in the PPOOLEX experiments to full scale are studied in the following by using dimensional analysis. A similar study has been performed earlier by Sonin (1981), which is reviewed first. Various dimensional analyses are then performed for phenomena occurring during the blowdown into the wetwell. Following the common practice in dimensional analysis, we refer to the experimental and full-scale facilities as model and prototype, respectively.

#### 3.1 Sonin (1981) analysis

Sonin (1981) considers the scaling of structural loads resulting from the discharge of steam at constant rate into the suppression pool of a BWR through a safety relief valve (SRV), as shown in Figure 5. The main difference between the SRV discharge and the discharge through the vent pipes in case of a LOCA is the discharge directly through the SRV piping in the former, rather than through the large drywell volume in the latter. In addition, the discharge device at the pipe outlet may be different for the SRV and vent pipes (e.g. a perforated pipe section in the former and a plain straight-cut pipe in the latter). However, the Sonin (1981) scaling analysis does not specify the discharge device at any point, but it is merely noted that the discharge devices may be of different types.

Sonin (1981) proposes that the pressure loads and other dependent variables, such as velocities, are completely specified by the set of quantities listed in Table 1. Thus, there are 16 independent variables and 4 reference dimensions. According to the Buckingham pi theorem, then,  $16 - 4 = 12$  independent dimensionless quantities can be formed. Sonin (1981) chooses the dimensionless terms listed in Table 2.



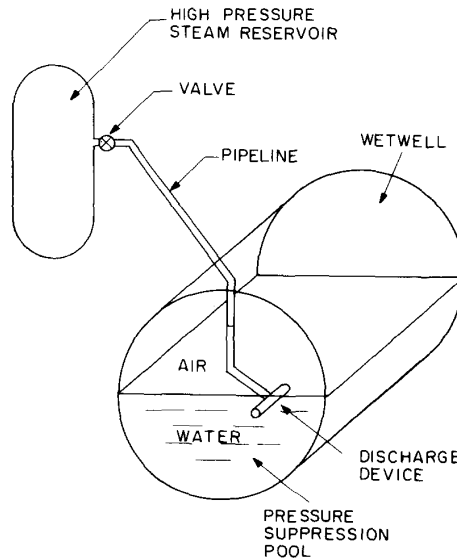


Figure 5. SRV / pool system. (Sonin, 1981)

Table 1. Independent quantities specifying the steam discharge into the water pool proposed by Sonin (1981).

Phenomenon	Variable		Units
Steam discharge conditions	$w_s$	steam mass flux based on pipe cross-sectional area	$\text{kg/m}^2\text{s}$
	$T_s$	steam reservoir temperature	K
Steam properties	$R_s$	specific gas constant	J/kgK
	$\gamma_s$	specific heat ratio	-
	$h_{fg}$	latent heat of condensation	J/kg
	$T_{sat}(\rho_w)$	saturation temperature at wetwell pressure	K
Pool conditions	$p_w$	pressure in pool at elevation of discharge	$\text{N/m}^2$
	$T_w$	bulk pool temperature	K
Water properties	$\rho_w$	reference water density at $T_w$	$\text{kg/m}^3$
	$c_w$	specific heat	J/kgK
	$\beta_w$	coefficient of thermal expansion	1/K
Thermal-hydraulic conditions in pipe	$\tau_p$	frictional shear stress on pipe wall	$\text{N/m}^2$
	$q_p$	heat flux to pipe wall	$\text{J/m}^2\text{s}$
Other quantities	$L$	characteristic length scale of system, e.g. pipe diameter	m
	$t$	time	s
	$g$	acceleration of gravity	$\text{m/s}^2$

Table 2. Similarity parameters used by Sonin (1981).

Phenomenon	Similarity parameter	Physical significance
Fluid properties	$\Pi_1 = \gamma_s$	specific heat ratio of steam
	$\Pi_2 = R_s / c_w$	~ specific heat ratio of steam and water
Water and steam dynamics	$\Pi_3 = \rho_w R_s T_s / p_w$	water density/steam density
	$\Pi_4 = w_s \sqrt{R_s T_s} / p_w$	dimensionless steam mass flow (~ Mach number)
Thermal and condensation phenomena	$\Pi_5 = c_w [T_{sat}(p_w) - T_w] / h_{fg}$	dimensionless water subcooling
	$\Pi_6 = R_s [T_s - T_{sat}(p_w)] / h_{fg}$	dimensionless steam superheat
	$\Pi_7 = R_s T_s / h_{fg}$	~ kinetic energy of steam at sound speed/latent heat
Time scale	$\Pi_8 = t \sqrt{p_w / \rho_w} / L$	dimensionless time
Pipe thermal hydraulics	$\Pi_9 = \tau_p / p_w$	shear stress on pipe wall/reference pressure
	$\Pi_{10} = q_p / c_w [T_{sat}(p_w) - T_w] / w_s$	dimensionless heat flux through pipe wall
Gravitational phenomena	$\Pi_{11} = \rho_w g L / p_w$	gravitational $\Delta p$ in water/reference pressure
	$\Pi_{12} = \beta_w [T_{sat}(p_w) - T_w] \rho_w g L / p_w$	pool buoyancy force parameter

Dimensionless local velocity and dimensionless local pressure on the pool wall can be subsequently expressed as a function of only the twelve dimensionless quantities:

$$\frac{v}{\sqrt{p_w / \rho_w}} = f(\Pi_1, \Pi_2, \dots, \Pi_{12}) \quad (9)$$

$$\frac{p_{wall}}{p_w} = g(\Pi_1, \Pi_2, \dots, \Pi_{12}) \quad (10)$$

Thus, if the dimensionless terms have the same numerical values in the model and in the prototype, the dimensionless velocity and pressure will be the same in the both systems.

The main assumptions made by Sonin (1981) are:

- The model and prototype are geometrically identical.
- Steam and water are used in both systems and both systems operate at the same thermodynamic conditions, i.e. pressures and temperatures.
- The steam mass flux based on the pipe cross-sectional area,  $w_s$ , is the same in both systems.
- Steam can be treated as ideal gas and water as simple liquid so that the steam and water thermodynamic properties are completely specified by the related quantities in Table 1. For instance, the saturation line is determined through the Clapeyron relation.
- The quantities  $\tau_p$  and  $q_p$  can be made the same by the experimenter in the model and in the prototype, although these are not strictly speaking independently specifiable quantities.

- The viscosity and thermal conductivity of steam and water do not affect explicitly the situation. For the steam, the effect of these properties inside the pipe is taken into account indirectly via  $\tau_p$  and  $q_p$ . The water outside the pipe is assumed to be in free turbulent shear flow, thus making the molecular diffusivities negligible.
- Gravitational effects can be considered secondary and, consequently,  $\Pi_{11}$  and  $\Pi_{12}$  can be neglected. The gravitational effects cannot be properly scaled when using steam and water as the fluids. For instance,  $\Pi_{11}$  remaining constant demands that  $\rho_w \sim L$ , which would have impractical consequences when trying to keep many of the other important pi-terms constant.

With these assumptions, all of the first ten similarity parameters will be same in both systems, if the model time is interpreted to scale as  $t \sim L$ . Thus, the scaling of the pressures and velocities becomes straight-forward. From Eqs. (9) and (10) we have that the local pressures and velocities will be the same in both systems, and from  $\Pi_8$  we have that time (e.g. pressure pulse duration and frequencies) will scale linearly with the system size.

In  $\Pi_8$ , the time scale of the system is defined as the ratio of length scale ( $L$ ) to velocity scale ( $\sqrt{p_w / \rho_w}$ ). This leads to time to scale as  $t \sim L$  when the velocities are same in the model and in the prototype. Thus, the same linear scaling for time applies also for the acoustic phenomena where the sound speed is the velocity scale.

The main conclusions made by Sonin (1981) are:

- The pressures, temperatures and velocities measured from the model are same as in full-scale at corresponding locations.
- The model time (e.g. pressure pulse duration and frequencies) scales in linear proportion to the system size.

The following issues are not addressed by Sonin (1981):

- The same fluid properties and velocities in both systems mean that the Reynolds numbers will smaller in the model, i.e.  $Re \sim L$ . However, the Reynolds numbers will be of the same order of magnitude when  $L$  is of the same order of magnitude. It is a somewhat common practice in scale-model testing to violate the  $Re$  similarity in favour of more important parameters (see Pankhurst, 1964; Young et al., 1997; Ishii et al., 1998).
- It is questionable whether the viscosity and thermal conductivity of the fluids can be neglected in the direct-contact condensation in the pool water during chugging.
- In the case of open vent pipes without perforated discharge device, gravitation may affect chugging (e.g. pressure amplitude through bubble size and frequency of chugging events). For the open vent pipes, the gravitational  $\Delta p$  caused by the submergence depth of the pipes may not be negligible.
- Transient heat transfer in the structural components.
- Effect of FSI, i.e. effect of the pool wall motion on the pressure loads. FSI has an effect at least in the PPOOLEX facility (Timperi, 2009).

### 3.2 Pressure loss in a pipe

Below we consider pressure loss in a pipe including minor pressure loss. The minor loss may be e.g. due to a valve in the pipe or, in the case of the vent pipe, due to the entrance loss where the vent pipe connects to the drywell. The pressure loss is expected to be a function of the following quantities (Young et al., 1997):

$$\Delta p = f(u, D, L, \varepsilon, \rho, \mu, K) \quad (11)$$

where  $u$  is the fluid velocity,  $D$  is the pipe diameter,  $L$  is the pipe length,  $\varepsilon$  is the pipe wall roughness,  $\rho$  the fluid density,  $\mu$  is the fluid viscosity and  $K$  is the minor loss coefficient. There are then 8 variables and 3 reference dimensions, and thus  $8 - 3 = 5$  independent dimensionless terms can be formed. Note that we have included the dependent variable (here  $\Delta p$ ) as one of the variables, so that the first pi-term will include the dependent variable. This is a common practice in dimensional analysis and differs slightly from the convention used by Sonin (1981).

We choose the following dimensionless quantities:

$$\begin{aligned} \Pi_1 &= \frac{\Delta p}{\frac{1}{2} \rho u^2} && \text{dimensionless pressure drop} \\ \Pi_2 &= \frac{\rho u D}{\mu} && \text{Reynolds number} \\ \Pi_3 &= \frac{L}{D} && \text{pipe length / pipe diameter} \\ \Pi_4 &= \frac{\varepsilon}{D} && \text{surface roughness / pipe diameter} \\ \Pi_5 &= K && \text{minor loss coefficient} \end{aligned}$$

For same velocities and fluid properties in the model and in the prototype, it is required that the second to fifth pi-terms be equal in order to have equal pressure drops. As in the Sonin (1981) analysis, the Reynolds number will scale as  $Re \sim L$  with these conditions. However, this is not necessarily severe violation of the similarity when  $L$  is of the same order of magnitude for the following reasons: i) for pipes with surface roughness and having sufficiently high Reynolds number, the friction coefficient is independent of  $Re$ , ii) the friction coefficient varies only mildly with  $Re$  for smooth pipes and iii) the minor loss coefficient is often practically independent of  $Re$  (Young et al., 1997). The pipe wall shear stress, used in the Sonin (1981) analysis, is same in the model and in the prototype in case of equal pressure drop in the pipe.

The total pressure drop with friction coefficient  $f$  is

$$\frac{\Delta p}{\frac{1}{2} \rho u^2} = \frac{fL}{D} + K \quad (12)$$

Thus, in case of different  $f$  in the model and in the prototype, the total pressure drop could be made same by varying  $K$ .

### 3.3 Vent clearing transient

In this section, we make a dimensional analysis of the initial vent clearing transient, which occurs at the beginning of the LOCA. Assumptions used in the analysis are the following:

- Air is compressible and governed by the ideal gas law, whereas water can be treated as incompressible.
- The viscosities of air and water can be neglected, since the event is dominated by the pressure and inertial effects.
- Gravitational effects are negligible.

The pool wall pressure is written as a function of the following quantities:

$$p_{wall} = f(p_g, p_w, T_g, T_w, R_g, \gamma_g, \rho_w, L, t) \quad (13)$$

where  $p_g$  is air pressure in the drywell,  $p_w$  is water pressure in the wetwell,  $T_g$  is air temperature in the drywell,  $T_w$  is water temperature in the wetwell,  $R_g$  is specific gas constant,  $\gamma_g$  is air specific heat ratio,  $\rho_w$  is water density,  $L$  is the system length scale and  $t$  is time. There are then 10 variables and 4 reference dimensions, and thus  $10 - 4 = 6$  independent dimensionless terms can be formed.

We choose the following dimensionless quantities:

$$\begin{aligned} \Pi_1 &= \frac{p_{wall}}{p_w} && \text{dimensionless wall pressure} \\ \Pi_2 &= \frac{p_g}{p_w} && \text{ratio of pressures in the drywell and wetwell} \\ \Pi_3 &= \frac{T_g}{T_w} && \text{ratio of temperatures in the drywell and wetwell} \\ \Pi_4 &= \frac{p_g}{R_g T_g \rho_w} && \text{ratio of air and water densities} \\ \Pi_5 &= \gamma_g && \text{specific heat ratio of air} \\ \Pi_6 &= \frac{t}{L} \sqrt{\frac{p_w}{\rho_w}} && \text{dimensionless time} \end{aligned}$$

It follows that the same conclusions can be drawn as in the Sonin (1981) analysis. The wall pressure will be same in both systems, if the fluid properties and the operation conditions (pressures and temperatures) are same, and the model time will scale as  $t \sim L$  according to  $\Pi_6$ . Note that this pi-term is same as in the Sonin (1981) analysis. Essentially similar but simplified analysis yielding the same conclusions can be performed by treating also air as incompressible.

### 3.4 Bubble rise in the pool

For the bubble rise, we consider the early acceleration phase where the water viscosity is of secondary importance. The bubble velocity  $u$  is written

$$u = f(D, \rho_g, \rho_w, t, g) \quad (14)$$

where  $D$  is the bubble diameter,  $\rho_g$  is the bubble gas density,  $\rho_w$  is the water density,  $t$  is time and  $g$  is the acceleration of gravity. There are then 6 variables and 3 reference dimensions, resulting in 3 dimensionless parameters. They are chosen here as follows:

$$\Pi_1 = \frac{ut}{D} \quad \text{dimensionless velocity}$$

$$\Pi_2 = \frac{\rho_g}{\rho_w} \quad \text{ratio of gas and water densities}$$

$$\Pi_3 = t \sqrt{\frac{g}{D}} \quad \text{dimensionless time}$$

The same fluid properties in the model and in the prototype ensures that the second term remains equal. From the third term, we have that time scales as  $t \sim D^{1/2}$ . Consequently, the first term requires that the bubble velocity scales as  $u \sim D^{1/2}$ .

This shows that the rise of the large bubbles in the water pool are miss-scaled in the Sonin (1981) analysis, where it is assumed that  $t \sim L$ . With the linear time dependency, the bubble would rise too slowly in the small scale compared to full scale. This is noted also by Sonin (1981) when he discusses the applicability of the analysis to the initial vent clearing transient with air.

### 3.5 Condensation water hammer

The volume acceleration caused by the large collapsing steam bubble is written

$$\ddot{V} = f(R, \Delta p, \rho, K) \quad (15)$$

where  $R$  is the bubble initial radius,  $\Delta p$  is the pressure difference between the bubble pressure and ambient water pressure far away from the bubble,  $\rho$  is the water density and  $K$  is the water bulk modulus. Note that the speed of sound in water is  $c = \sqrt{K/\rho}$ . With 5 variables and 3 reference dimensions,  $5 - 3 = 2$  pi-terms can be formed. We choose

$$\Pi_1 = \frac{\rho \ddot{V}}{R \Delta p} \quad \Pi_2 = \frac{K}{\Delta p} \quad (16)$$

Thus, with same water properties and pressure difference, we have that the volume acceleration scales linearly with the system size:  $\ddot{V} \sim R$  (here we assume that the bubble size  $R$  is directly proportional to the system size).

The pressure amplitude at distance  $r$  from the bubble is (Pättikangas et al., 2011)

$$p = \frac{\rho \ddot{V}}{4\pi r} \quad (17)$$

From this and Eq. (16) we see that with same water properties and pressure difference, the pressure amplitude is independent of the system size. This is consistent with the numerical simulations of the bubble collapse by Timperi et al. (2012).

For the collapse time of the bubble, we write

$$t = f(R, \Delta p, \rho) \quad (18)$$

Here the compressibility effects (i.e. the water bulk modulus  $K$ ) have been neglected since they affect only at the very late phase of the collapse when the water velocity near the bubble

grows high (see Pättikangas et al., 2011). With 4 variables and 3 reference dimensions, we have  $4 - 3 = 1$  pi-terms. We choose

$$\Pi_t = \frac{t}{R} \sqrt{\frac{\Delta p}{\rho}} \quad (19)$$

From the analytical solution in Pättikangas et al. (2011), the collapse time is

$$t = 0.915R \sqrt{\frac{\rho}{\Delta p}} \quad (20)$$

This is consistent with Eq. (19). Thus, the collapse time depends linearly on the system size:  $t \sim R$ , which is also consistent with the numerical simulations by Timperi et al. (2012). These scalings, i.e. the pressure amplitude remaining constant with system size and time scaling linearly, are same as in the Sonin (1981) analysis.

The dimensional analysis may also be performed directly for the pressure amplitude caused by the collapse. We write

$$p = f(R, \Delta p, \rho, K) \quad (21)$$

and have again  $5 - 3 = 2$  pi-terms. We choose

$$\Pi_{p1} = \frac{p}{\Delta p} \quad \Pi_{p2} = \frac{K}{\Delta p} \quad (22)$$

Thus, we have that the pressure amplitude is independent of the water density or the system size, which is consistent with Eqs. (16) and (17). Since the sonic velocity is  $c = \sqrt{K/\rho}$ ,  $\Pi_{p1}$  and  $\Pi_{p2}$  remaining constant requires  $p \sim K \sim c^2$ . Thus, the sonic velocity has a large effect on the pressure amplitude. This effect is caused by the compressibility of water starting to restrict water velocity near the bubble in the late phase of the collapse (when the Mach number becomes significant), resulting in decreased volume acceleration and thus in decreased pressure amplitude when the sonic velocity is decreased (see Pättikangas et al., 2011). Effect of the sonic velocity on the pressure pulse was studied numerically in Timperi et al. (2012) by varying the sonic velocity and holding the other variables constant. Then we found for the pressure amplitude  $p \sim c$ . However, the present dimensional analysis shows that the both  $\Pi_{p1}$  and  $\Pi_{p2}$  remaining constant would have required also varying the pressure difference with the sonic velocity as  $\Delta p \sim c^2$  in the simulations. This results correctly in  $p \sim c^2$ .

The compressibility of water has an effect on the duration of the pressure pulse, although it could be neglected for the collapse time. For the duration of the pulse, we write

$$t_{pulse} = f(R, \Delta p, \rho, K) \quad (23)$$

and we choose  $5 - 3 = 2$  dimensionless terms:

$$\Pi_{t1} = \frac{t_{pulse}}{R} \sqrt{\frac{\Delta p}{\rho}} \quad \Pi_{t2} = \frac{K}{\Delta p} \quad (24)$$

The first term is essentially the same as  $\Pi_t$  above, while the second is the same as  $\Pi_{p2}$ . Thus, as for the collapse time, we have  $t_{pulse} \sim R$ , which is again consistent with the

numerical simulations by Timperi et al. (2012). The second term may also be written  $\Pi_{12} = \rho c^2 / \Delta p$ . Thus, the both terms remaining constant requires that  $t_{\text{pulse}} \sim 1/\sqrt{\Delta p} \sim 1/c$ .

The scaling of the pressure amplitude may also be checked by considering energy balances. Energy released in the collapse is proportional to the bubble volume  $V$  and pressure difference:

$$E \sim V\Delta p \quad (25)$$

On the other hand, it can be shown analytically that for strain energy in water due to the acoustic pressure pulse of amplitude  $p$ , we may write

$$E_\varepsilon \sim \frac{\lambda r^2 p^2}{K} \quad (26)$$

where  $\lambda$  is the wave length of the pulse and  $r$  is distance from the bubble. Assuming that the bubble size is directly proportional to the system size  $L$  and that the pulse duration scales as above  $t_{\text{pulse}} \sim L$ , i.e. for same sonic velocity  $\lambda \sim L$ , the energies may be written

$$E \sim L^3 \Delta p \quad (27)$$

$$E_\varepsilon \sim \frac{L^3 p^2}{K} \quad (28)$$

From these we see that when the pressure difference and bulk modulus are same in both systems, the pressure amplitude is indeed independent of the system size as above. It is also seen that the pulse duration is an important parameter as it determines the span over which the released energy is spread, thus affecting the pressure amplitude.

In the above dimensional analyses of the bubble collapse, we neglected the following effects:

- The possible small amount of non-condensable gas in the bubble.
- Steam in the bubble and the condensation phenomena.
- The possible breaking of the bubble into a two-phase mixture in the late phase of the collapse.

The experimental pressure peaks have been much lower and wider than in the simulations using the idealized assumptions, as shown in Sec. 2 and in Timperi et al. (2012). Thus, some of the three neglected phenomena may have a significant effect on the pressure pulse.

### 3.6 Single-phase mass and energy flow scaling

Below we consider the change in mass and energy in a fixed volume  $V$  due to in- and out-flow of ideal gas, which may be e.g. air or steam. The mass balance equation is

$$\frac{dm}{dt} = \sum_i \dot{m}_i \quad (29)$$

where  $m$  is mass in the volume and  $t$  is time. The mass flow rate at duct  $i$  is

$$\dot{m}_i = \rho_i u_i A_i \quad (30)$$



where  $\rho_i$  and  $u_i$  are the area-averaged density and velocity, respectively, and  $A_i$  is the surface area. For fixed volume  $V$ , the mass balance becomes

$$V \frac{d\rho}{dt} = \sum_i \rho_i u_i A_i \quad (31)$$

where  $\rho$  is the volume-averaged density in the vessel. The variables are non-dimensionalized as follows:

$$V^* = \frac{V}{V_0} \quad A^* = \frac{A}{A_0} \quad t^* = \frac{t}{t_0} \quad \rho^* = \frac{\rho}{\rho_0} \quad u^* = \frac{u}{u_0} \quad (32)$$

where the sub-index 0 refers to the reference values. Inserting these into Eq. (31) yields after some manipulation a non-dimensional mass balance

$$\Pi_m V^* \frac{d\rho^*}{dt^*} = \sum_i \rho_i^* u_i^* A_i^* \quad (33)$$

where

$$\Pi_m = \frac{V_0}{u_0 A_0 t_0} \quad (34)$$

Thus, the non-dimensional mass balance equation is the same for the model and for the prototype, if the dimensionless term  $\Pi_m$  is the same in both systems. This occurs if the reference velocities are same and the other quantities scale as

$$V_0 \sim L^3 \quad A_0 \sim L^2 \quad t_0 \sim L \quad (35)$$

It follows then that the single-phase mass flow scales correctly for the Sonin (1981) analysis. The same density  $\rho^*(t^*)$  leads to same pressures in the model and in the prototype when the both systems operate at the same thermodynamic conditions, as in the Sonin (1981) analysis.

For the energy flow scaling, we start from the energy balance equation with the potential and kinetic energy terms neglected (Wulff, 1996) and neglect further the heating/cooling and mechanical work terms:

$$V \frac{d\rho e}{dt} = \sum_i \rho_i u_i A_i h_i \quad (36)$$

where  $e$  is the volume-averaged specific internal energy and  $h_i$  is the area-averaged specific enthalpy. Following Wulff (1996), the energy balance is re-written by using the mass balance equation and relation  $h = e + p/\rho$ :

$$V\rho \frac{de}{dt} = \sum_i \rho_i u_i A_i (h_i - h) + \frac{p}{\rho} \sum_i \rho_i u_i A_i \quad (37)$$

In addition to the normalizations in Eq. (32), the following are used (Wulff, 1996):

$$e^* = \frac{e - e_{\min}}{c_v \Delta T} \quad h^* = \frac{h - h_{\min}}{c_p \Delta T} \quad p^* = \frac{p}{p_0} \quad (38)$$

where  $c_v$  and  $c_p$  are the specific heats at constant volume and pressure, respectively, and the reference temperature difference is  $\Delta T = T_{\max} - T_{\min}$ . The normalizations for  $e$  and  $h$  guarantee that the normalized first derivatives also are of order unity, when the minimum values of  $e$  and  $h$  are non-zero. Inserting into Eq. (37) yields a non-dimensional energy balance

$$\Pi_{e1} V^* \rho^* \frac{de^*}{dt^*} = \sum_i \rho_i^* u_i^* A_i^* (h_i^* - h^*) + \Pi_{e2} \frac{p^*}{\rho^*} \sum_i \rho_i^* u_i^* A_i^* \quad (39)$$

where

$$\Pi_{e1} = \frac{V_0 c_v}{u_0 A_0 t_0 c_p} \quad \Pi_{e2} = \frac{p_0}{\rho_0 c_p \Delta T} \quad (40)$$

For the same reference velocities and thermodynamic conditions as well as for scalings in Eq. (35), these dimensionless terms are same in the model and in the prototype, and thus the single-phase energy flow scales correctly for the Sonin (1981) analysis. The energy balance equation may be adapted also to the pool water energy inventory to yield the same result for the energy flow scaling of the steam latent heat flow into the pool water.

## 4. Description of the numerical model for a BWR containment

---

### 4.1 Simplified model

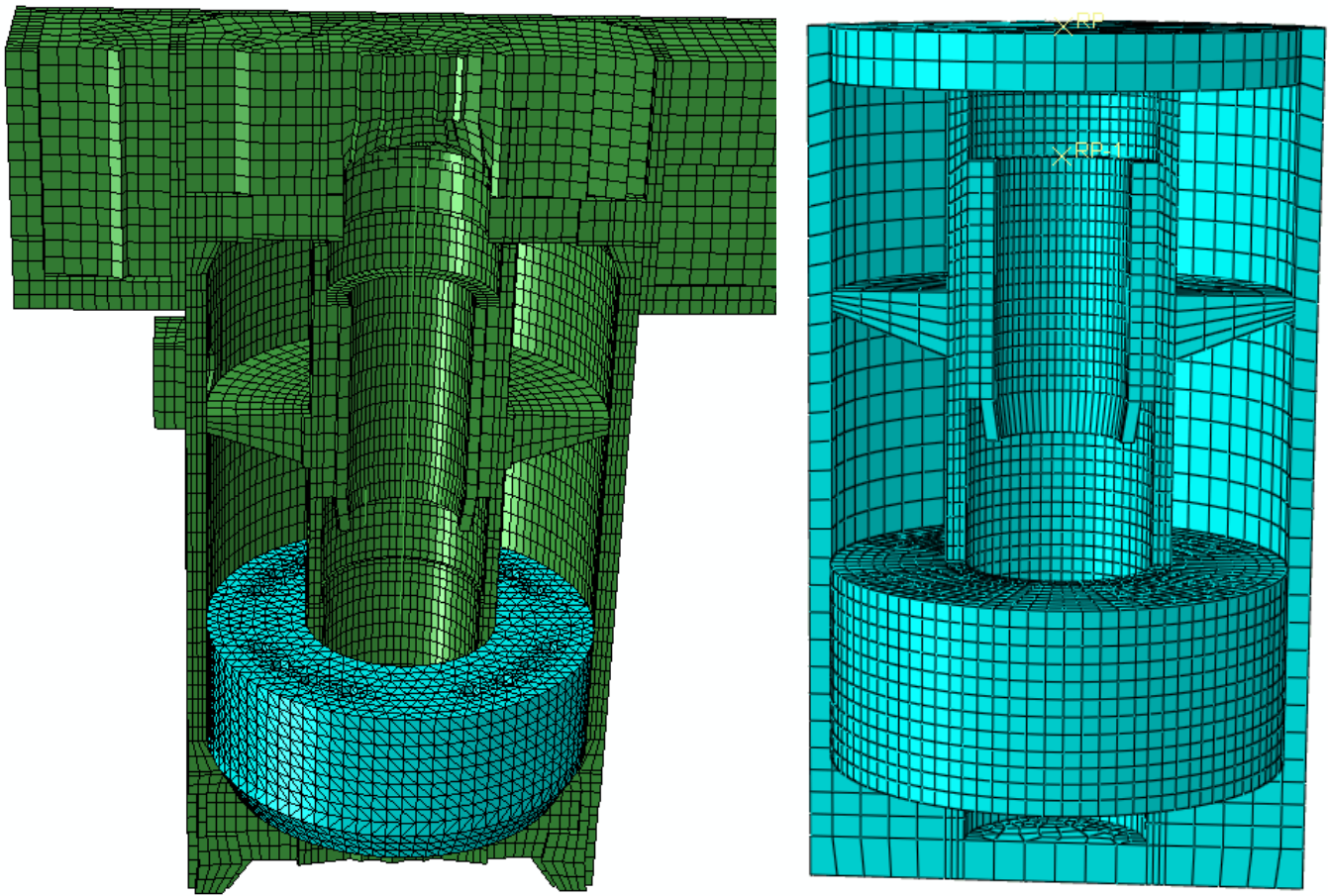
During 2011, preliminary computations of chugging phenomenon were performed with detailed model of the containment (Timperi et al. 2012). The use of the detailed model practically prevented the computation of the structural response during multiple chugging events due to the long computation time caused by the large number of elements in the model. The detailed model, used in the previous study, consisted of 68000 structural brick elements (type C3D8R in ABAQUS) and of 48000 acoustic elements (type AC3D8 and AC3D4 in ABAQUS). The total number of elements in the detailed containment model is roughly 116 000.

In order to study the response during multiple chugging events with varying desynchronization time, simplified model geometry was created, which in conjunction with the use of the explicit time integration enabled the computation of multiple events. Vertical cross-sections of the previous, detailed containment and simplified model geometry are presented in Figure 6a and Figure 6b, respectively. The water tanks located above the reactor pressure vessel are removed from the simplified model geometry and are substituted with a point mass, which is attached to the top surface of the containment with the Coupling-command in ABAQUS. In addition, complicated geometries, such as the domed shell above the RPV, that increase the amount of elements in the model are removed from the simplified geometry, see Figure 8a and Figure 8b. Removing the hollow parts and wholes from the bottom of the containment, results in increased rigidity.

The shape of the cross-section of the vent pipes in the wet well is changed from circular to square in order to enable regular meshing and thus decrease the number of element. However, the area of the vent pipe cross-section corresponds approximately to that of the actual containment, see Figure 7. As the chugging occurs in the wet well, located at the lower middle part of the containment, it was assumed that the containment experiences the highest loading in that area, and the geometry of that area was kept as close to the original as possible. However, the main focus of this study is in modeling the chugging phenomena realistically, not the exact values of maximum stress occurring in an actual containment.

In addition to simplifying the geometry, part of the containment were meshed using continuum shell elements with five section points through the thickness, instead of structural brick elements. Continuum shell elements appear to be three-dimensional continuum solids, but their kinematic and constitutive behavior is similar to conventional shell elements. Unlike conventional shell elements, continuum shell elements can be used to discretize an entire three-dimensional body. They allow finite membrane deformation and large rotations and can thus be used for nonlinear geometric analysis. Continuum shell elements use bending strain measures that are approximations to Koiter-Sanders shell theory, according to which displacement field normal to the shell surface does not produce any bending moments, e.g. radial expansion of a cylindrical shape will result only in membrane stress and strains. Since there is no variation through the thickness, there is no bending. (Abaqus, 2012)

The total number of elements in the simplified model is 21 715, consisting of 8032 linear hexahedral acoustic elements (type AC3D8R in ABAQUS), 1508 linear hexahedral continuum shell elements (type SC8R in ABAQUS), 12173 linear hexahedral continuum elements (type C3D8R) and two mass elements. Thus the number of elements in the simplified model geometry is more than five times smaller compared to the detailed model of the containment.



a)

b)

Figure 6. a) Detailed containment model used in the previous study (see Timperi et al., 2012). b) The model with simplified geometry.

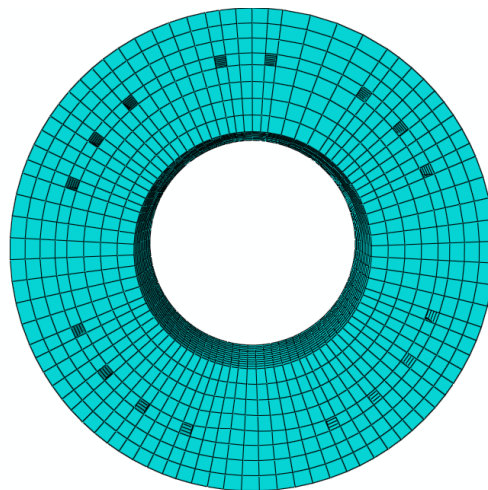


Figure 7. Simplified model geometry: meshed water in the wet well with square shaped vent pipe cross-section.

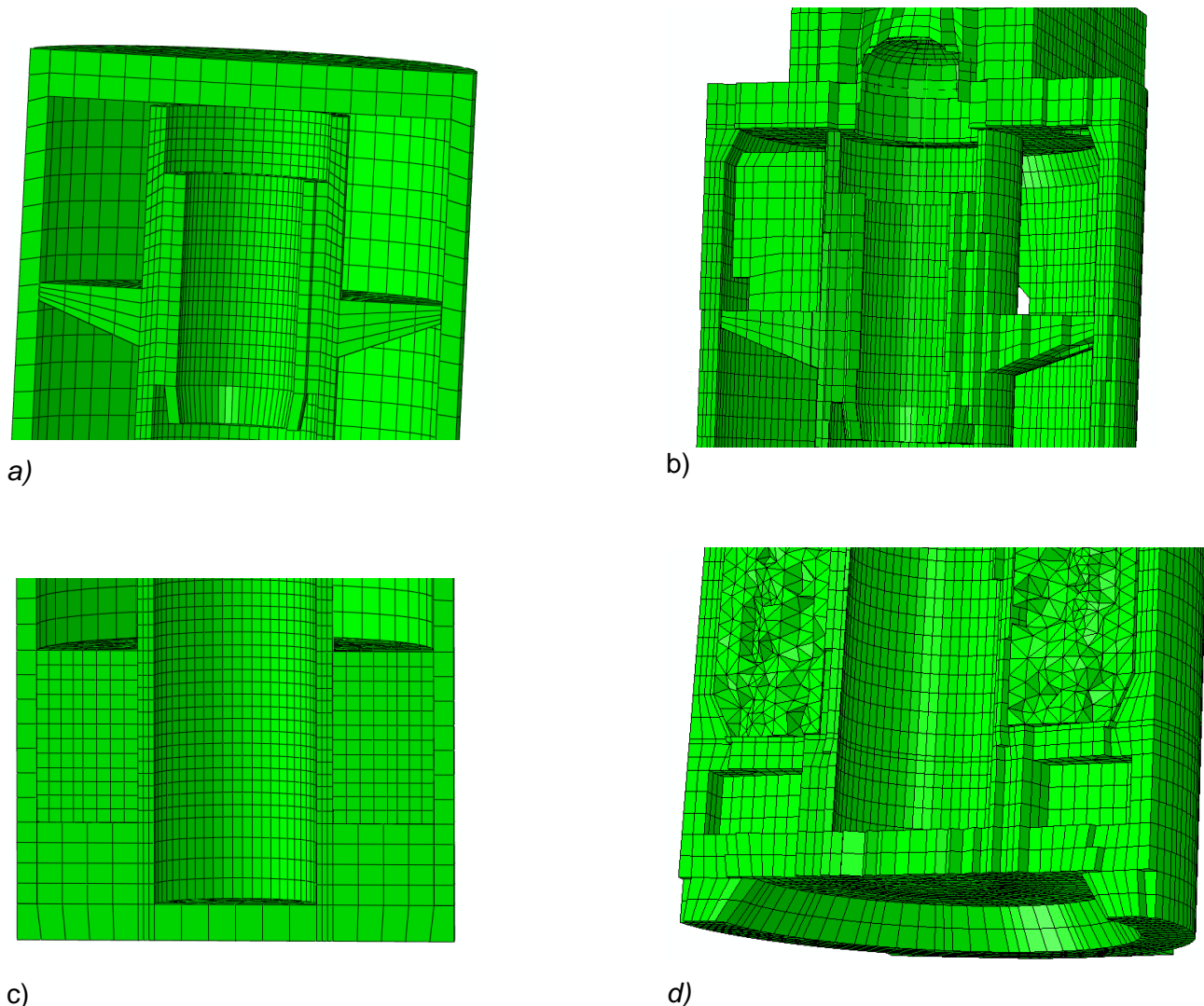


Figure 8. a) The upper part of the containment of the simplified model geometry. b) Upper part of the whole containment model. c) Lower part of the containment of the simplified model geometry. d) Lower part of the whole containment model.

The displacements of the bottom of the containment are restricted in x- y and z- directions, but rotations are allowed. Same boundary conditions were applied for the detailed model of the containment. The material properties, obtained from previous study (Timperi et al. 2012), used in the analysis are presented in Table 3. The total mass of the model with simplified geometry is  $3.26E+07$  kg, which equals the mass of the detailed model of the containment. The computations were performed with and without Rayleigh damping, of whose parameters are also presented in Table 3 and which is shown with respect to frequency in Figure 9. Thus, altogether four computation cases were considered:

1. Synchronized loading, material damping included
2. Desynchronized loading, material damping included
3. Synchronized loading, no material damping
4. Desynchronized loading, no material damping

Table 3. Material properties

Property	Concrete	Water
<b>Damping</b>		
Alpha	5.89	-
Beta	9.95E-05	-
Density [kg/m <sup>3</sup> ]	2400	1000
Young's modulus [Mpa]	39000	-
Poisson's ratio	0,17	-
Bulk modulus [Mpa]	-	2224
Speed of sound in the water [m/s]		1491

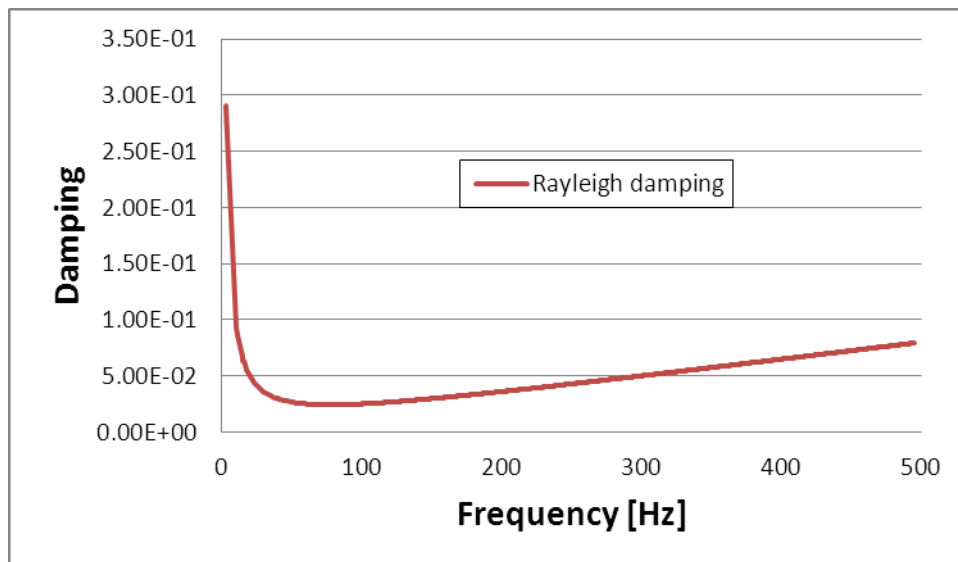


Figure 9. Rayleigh damping for concrete.

## 4.2 Analysis type

A finite element model of the containment was utilized in the attempt to model the effect of desynchronization. The analyses were carried out using implicit and explicit dynamic analyses. The implicit dynamic analysis is expensive, since a set of non-linear dynamic equilibrium equations are solved at each time increment. The explicit dynamic analysis is computationally efficient for the analyses of large models and for the analysis of extremely discontinuous events or processes. It also allows the models to undergo large rotations and large deformations or geometrically linear deformation theory. The explicit time integration is an efficient way for solving a large number of small time increments. It uses an explicit central-difference time integration rule, where each increment is relatively inexpensive compared to the direct-integration dynamics procedure (implicit dynamics), because there is no solution for a set of simultaneous equations. The explicit dynamics procedure uses explicit integration rule together with the use of diagonal element mass matrices. The equation of motions for the body is integrated as follows:

$$\dot{u}_{(i+\frac{1}{2})}^N = \dot{u}_{(i-\frac{1}{2})}^N + \frac{\Delta t_{(i+1)} + \Delta t_{(i)}}{2} \ddot{u}_{(i)}^N, \quad (41)$$

$$u_{(i+\frac{1}{2})}^N = u_{(i-\frac{1}{2})}^N + \Delta t_{(i+1)} \dot{u}_{(i)}^N, \quad (42)$$

where  $u^N$  is a degree of freedom and the subscript  $i$  is the increment number of a step. The equation is explicit since that the kinematic state of the next increment is solved using the known values of  $\dot{u}_{(i-\frac{1}{2})}^N$  and  $\ddot{u}_{(i)}^N$  previous increment. Computational efficiency is obtained by

using diagonal element mass matrices, because the acceleration at the beginning of the increment are computed by:

$$\ddot{u}_{(i)}^N = (M^{NJ})^{-1} (P_{(i)}^J - I_{(i)}^J), \quad (43)$$

where  $M^{NJ}$  is the mass matrix,  $P^J$  is the applied load vector and  $I^J$  is the internal force vector. An inverse of the lumped mass matrix is simple to compute and the vector multiplication of the mass inverse by the inertial force requires only same number of operations as there are degrees of freedom in the model and therefore the lumped mass matrix is used. No iterations and tangent stiffness matrixes are needed in the explicit dynamics procedure. (Abaqus, 2012)

### 4.3 Analysis comparison

In order to study whether the behavior of the containment can be computed using explicit dynamics analysis procedure, a short period of chugging phase was computed using also implicit dynamics analysis procedure and the structural responses obtained with both methods were compared. The simplified model geometry was utilized in both cases. The total number of elements used in the implicit dynamic procedure was equal to that in the explicit model.

The radial displacements were computed from four different nodes. The nodes are located approximately every 90° around the containment, at the height were chugging causes wall movement. The locations of the nodes are presented in Figure 10 and the computed radial displacements in Figure 11a-d. Since the comparison shows very good match, it was considered that explicit dynamics can be used with reasonable accuracy.



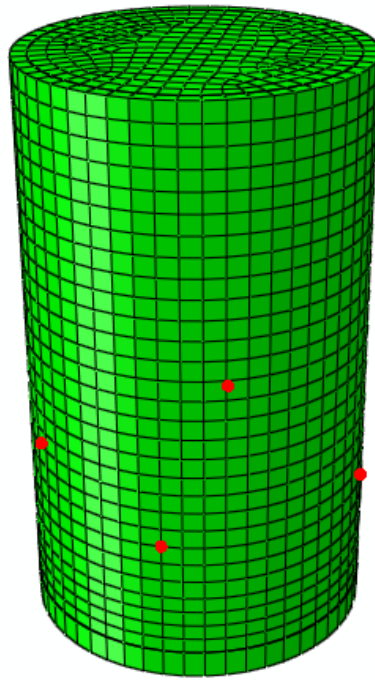


Figure 10. Location of nodes 3144, 142, 1338 and 131.

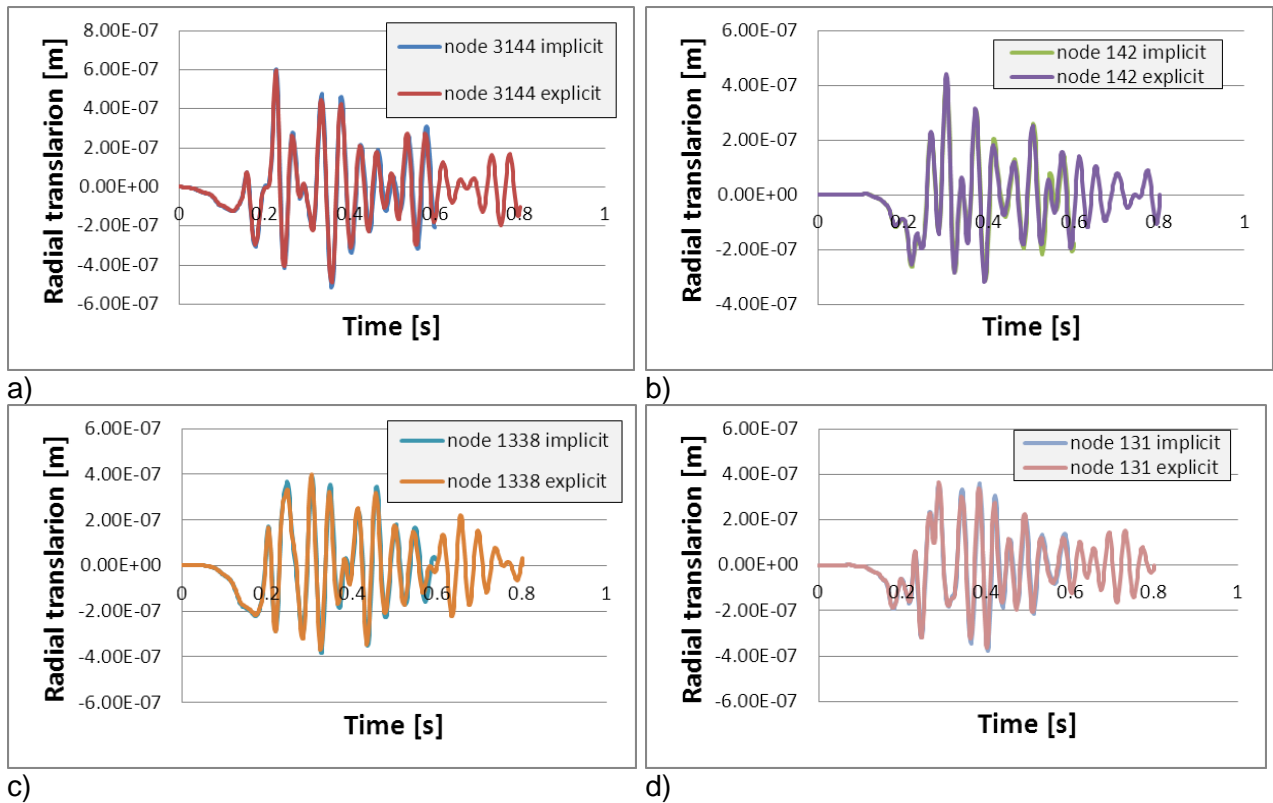


Figure 11. Radial displacements at nodes 3144, 142, 1338 and 131 obtained with implicit and explicit dynamics.



## 5. Desynchronization characteristics

---

Kukita and Namatame (1985) claimed that there exists an efficient synchronization mechanism, which is limited by the maximum speed of fluid dynamics perturbation, that is, the speed of sound. In turn, the speed of sound in the water is affected, for instance, by the amount of bubbles in the water (Björndahl and Andersson, 1998). However the computed transit time for an acoustic wave through the pool water is considerably shorter than the standard deviation of desynchronization time. Kukita and Namatame concluded that the pool natural frequency affects the effective transit time of an acoustic perturbation. Kukita and Namatame also observed that the effect of vent spacing to the desynchronization is weak, although it seems to exist. It is finally concluded, that even though it is commonly assumed that the bubble condensation process is independent from the pool geometry and hydrodynamic interactions among the vent pipes, but since the process is inertia controlled, it must be influenced by the surrounding pressure field, which in turn is dependent on the pool geometry as well as chugs occurring at other vent pipes.

In addition to desynchronization time, two characteristic variables are identified that influence the magnitude of the pool boundary load. The three variables are:

1. Desynchronization between chugging events between different pipes,
2. Chugging repeating interval
3. Duration of the chug event.

In large-scale seven-vent pipe test (Kukita and Namatame, 1985) performed with JAERI test facility, the standard deviation was determined to be 42ms for large chugs, for which the pool boundary load amplitude was larger than 10 kPa, whereas in small-scale two-vent experiment, PAR-10, performed with PPOOLEX test facility the standard deviation of desynchronization time is determined to be 13,6ms (Timperi et al. 2012), when similar method to that used by Kukita and Namatame is applied in the determination of an individual desynchronization time. The determination of desynchronization time is illustrated in Figure 12, where a mean time,  $t_{ave}$ , for two separate chugs is determined and desynchronization time is determined as the time difference,  $\Delta t$ , between the mean value and an individual peak under pressure. The average time between chugs occurring at the same vent-pipe outlet in the PAR-10 experiment was computed to be 1.75 s whereas in the test data obtained with the JAERI test facility, the corresponding value is approximately 2 s. The third characteristic variable, duration of the chug event, is determined as the duration from steady state pressure to peak pressure. Value obtained from a representative chug from experiment COL-01, is less than 0.01s. The COL-01 is a single-vent experiment, but similar values were also obtained from experiment PAR-10, in which two vent-pipes are used. It is noteworthy, however, that in some PPOOLEX experiments clearly longer chug events have been observed. In the seven-vent experiments performed at JAERI, the duration of the chug event is 0.15 s. The geometrical differences of the PPOOLEX and JAERI test facilities are presented in Table 4.

The statistics obtained from the JAERI test facility was concluded to be representative for the 16 vent pipe containment, due to the large number of vent pipes in both cases. Thus, the standard deviation for the desynchronization time was assumed to be 42 ms. Chugging repeating interval and duration of the chug event were assumed to be 2 s and 0.15 s, respectively. However, the shape of the chug event was taken from a representative event in COL-01 experiment.

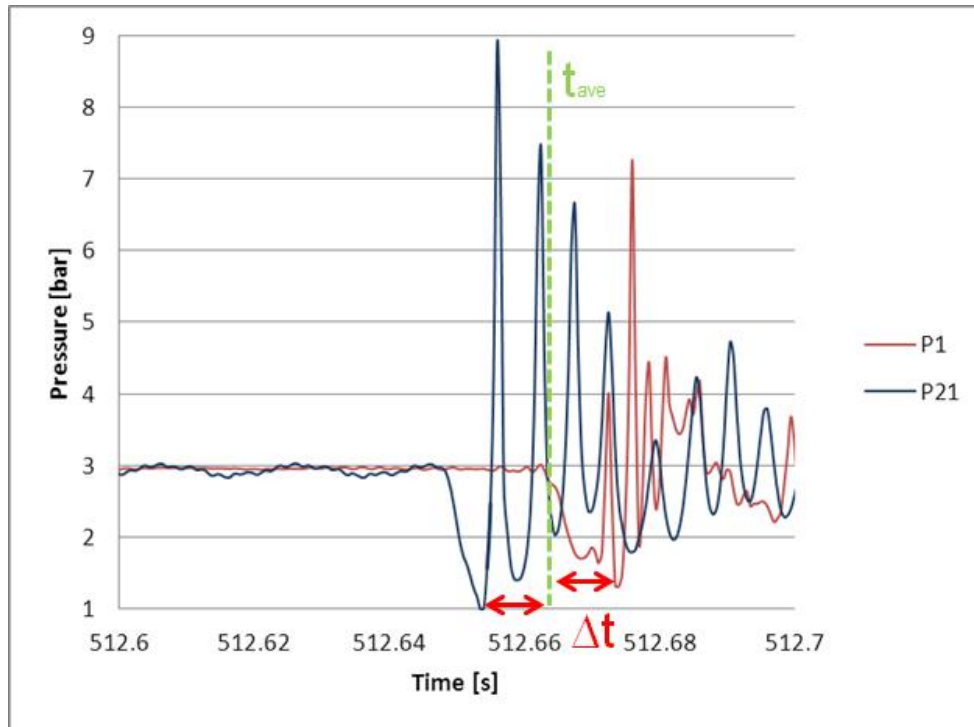


Figure 12. Schematic illustrating the determination of desynchronization time, data from experiment PAR-10.

Table 4. Geometrical differences between PPOOLEX and JAERI test facilities.

	Number of pipes	Pipe $D_o$	Distance between pipes	
			Min distance [m]	Max distance [m]
PPOOLEX	2	0.2	0.5	0.5
Jaeri	7	0.6	1.2	4.7

## 6. Description of the loading

Since the desynchronization time is not constant, the structural response was studied during multiple chugging events, in which the desynchronization time varies. The desynchronization times were obtained by creating a normal distribution with mean value being zero and standard deviation 0.042 s. Out of this distribution, altogether 1600 initiation times (100 per pipe) were determined using Matlab's Random-function, which gives randomly selected values out of given distribution.

The initiation times were then ordered in 100 groups, each containing 16 initiation times. For every group, the minimum value was determined and added to each member of that group, so that the first initiation time was 0, in every group. Then  $(n-1)*2$  seconds, were added to the initiation times of each group, where  $n$  is the order number of the group. For example, for the 6<sup>th</sup> group, the added time is  $(6-1)*2=10$  seconds.

The loading in the finite element analyses is created as volume acceleration, as used in the previous studies concerning fluid-structure interaction (FSI) computations (Pättikangas et al., 2011). The volume acceleration amplitudes for 1600 chugs were written using in-house codes.

The location of the vent pipes and their number is shown in Figure 13 and volume acceleration functions from time 0-4s in Figure 14.

In addition to asynchronous loading, an analysis in which the loading occurred simultaneously in all 16 vent pipes was performed. In order to study, whether the response of the structure changes with time, multiple chugging events were considered also in that case.

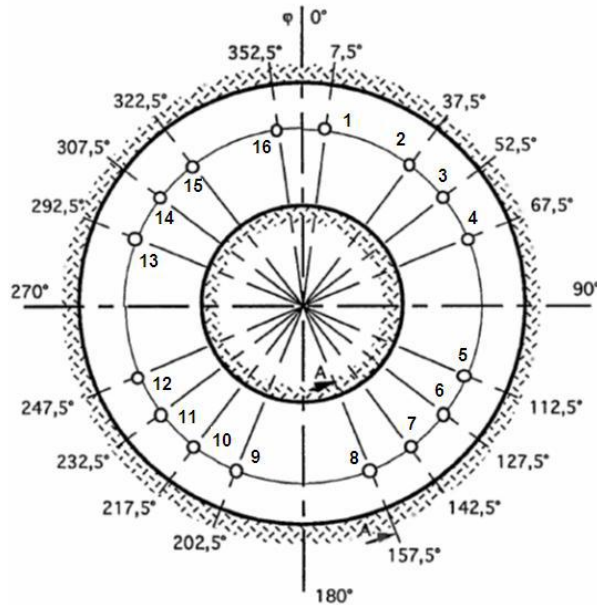


Figure 13. Location and number of vent pipes.

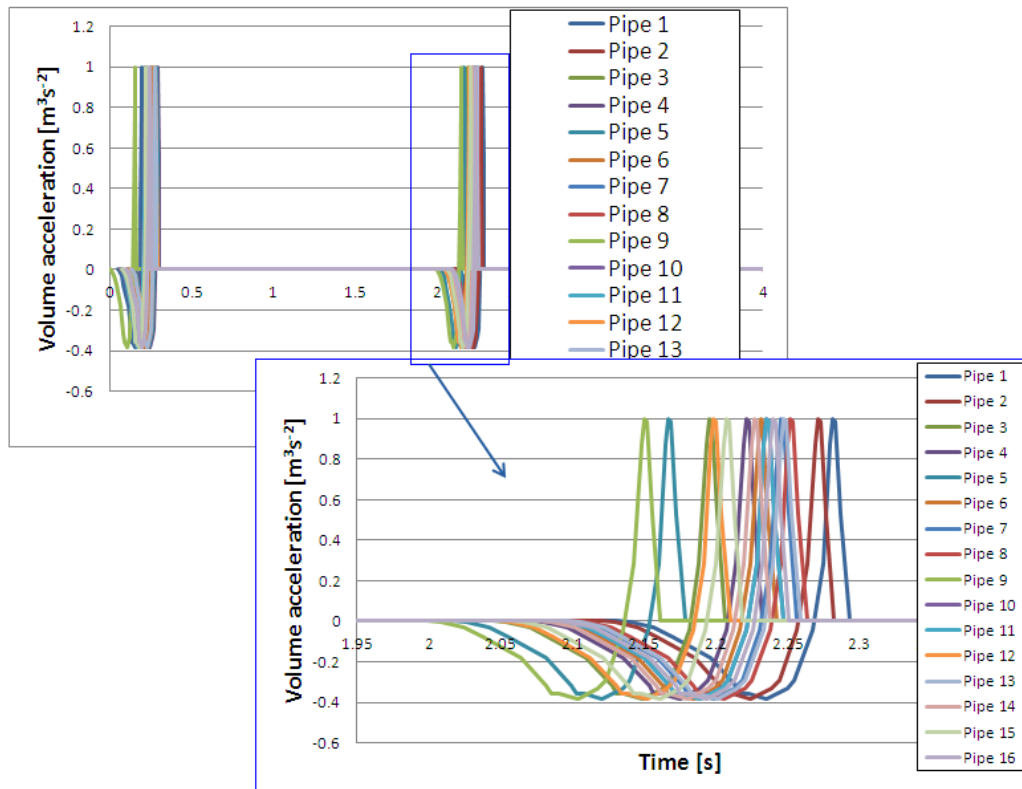


Figure 14. Example of volume acceleration functions from time 0-4s.

## 7. Results and discussion

### 7.1 Structural response during chugging

Due to relatively long simulation period and small analysis time increment, the size of the result files grows very large. In-house codes were created and utilized to gather displacement and von Mises stress data from the area of interest. The elements and nodes for which the von Mises stress and radial displacements were computed are presented in Figure 15(a) and Figure 15(b), respectively. Maximum and root mean squared (RMS) values were determined from both quantities. The RMS value is used for the determination of the location, which experiences largest variance in the von Mises stresses/displacements during the simulation time. The RMS value for discrete distribution is computed as follows:

$$R(x) = \sqrt{\frac{\sum_{k=0}^N x_k^2}{N}}, \quad (44)$$

where  $N$  is the number of samples.

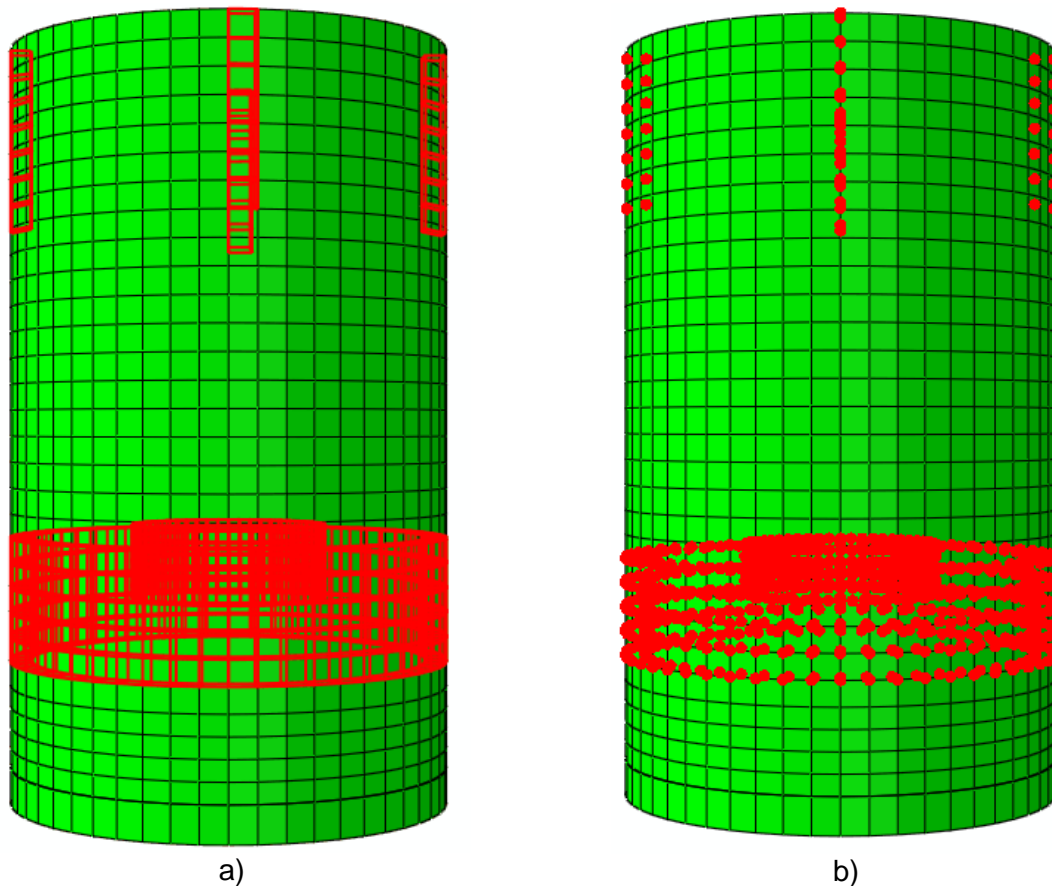


Figure 15. a) Elements and b) nodes for which the von Mises stress and displacements were computed.

Since the containment is in the Cartesian coordinate system and radial displacements were of interest, coordinate transformation was performed. The radial displacement for node  $i$ , taking place in the x-y-plane is computed as follows:

$$r_i = \frac{x_i u_i + y_i v_i}{\sqrt{x_i^2 + y_i^2}}, \quad (45)$$

where  $x_i$  and  $y_i$  are x- and y-coordinates of the node,  $u_i$  and  $v_i$  are the displacements in the x- and y- direction, correspondingly.

The maximum von Mises stress, maximum radial displacement, their time of occurrences and maximum RMS values of both quantities for four considered cases are presented in Table 5.

*Table 5. Computed maximum von Mises stresses, displacements, their time of occurrences and RMS values for four considered cases.*

	1. Synchronous loading	2. Desynchronized loading	Difference %	3. Synchronous loading, no material damping	4. Desynchronized loading, no material damping	Difference %
<b>Max von Mises [Pa]</b>	5097	3424	33	5262	5099	3
<b>Time of occurrence</b>	0.159582	28.2729		0.218523	28.2728	
<b>Max RMS von Mises</b>	1318	430	67	1893	1211	36
<b>Max Displacement [m]</b>	1.32E-06	1.15E-06	13	1.72E-06	2.20E-06	-28
<b>Time of occurrence</b>	6.23984	56.2859		86.2813	182.266	
<b>Maximum RMS displacement</b>	3.39E-07	1.24E-07	63	6.04E-07	4.66E-07	23

The results show that the desynchronization of chugging decreases the maximum stresses significantly for the case in which material damping is included; the maximum stress for asynchronous loading being 33% smaller than for the case in which chugging takes place synchronously in all 16 vent pipes. When the material damping is omitted, the difference between the maximum stresses for the two loading types decreases significantly, the maximum von Mises stress being only 3% lower for the desynchronized case. Thus the damping is a significant factor concerning the maximum loading. The maximum displacement is actually higher for the desynchronized loading, when material damping is omitted.

The difference between responses for synchronized and desynchronized loading and damped and un-damped material can be seen in Figure 16, where radial displacements for all cases during time 0-10s are presented for those nodes in which the maximum value occurred. It can be seen that for the un-damped material, the motion caused by the previous chugs has not ceased as a new group of chugs takes place. In case 1, in which material damping is considered and loading is synchronized, the same displacement interval is repeated for every chugging event. This is not the case for either of the desynchronized loading cases, because the loading is different for every chugging events, whereas in case 3, where loading is synchronized but material damping is omitted, the response is not constant for every chugging event due to the motion of the containment.

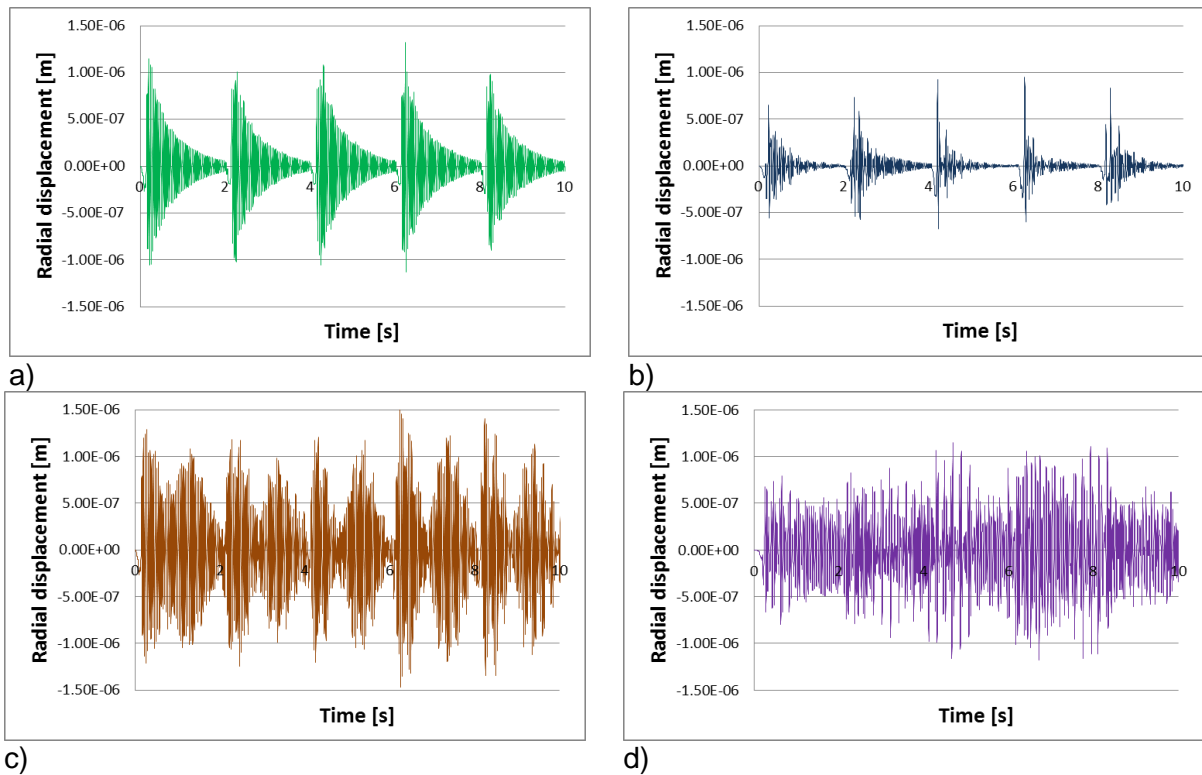


Figure 16. Radial displacements during 0-10s for nodes in which the maximum displacements during the whole analysis occurs for a) synchronized loading and material damping, b) desynchronised loading and material damping, c) synchronized loading, no material damping and d) desynchronised loading, no material damping.

In order to study the frequency of the impulse, a fast Fourier transformation was performed on the radial displacement data of the node which experienced the maximum value in case 4 (undamped, desynchronized loading). In order to set the damping for the frequencies of the impulses, the coefficients of the Rayleigh damping have to be modified. The fast Fourier transformation and modified Rayleigh damping are presented in Figure 17. It can be seen that the highest peaks are located between 3-30Hz. These values are used for the determination of Rayleigh damping coefficients, which are  $\alpha = 1.781$  and  $\beta = 5.07E - 04$ .

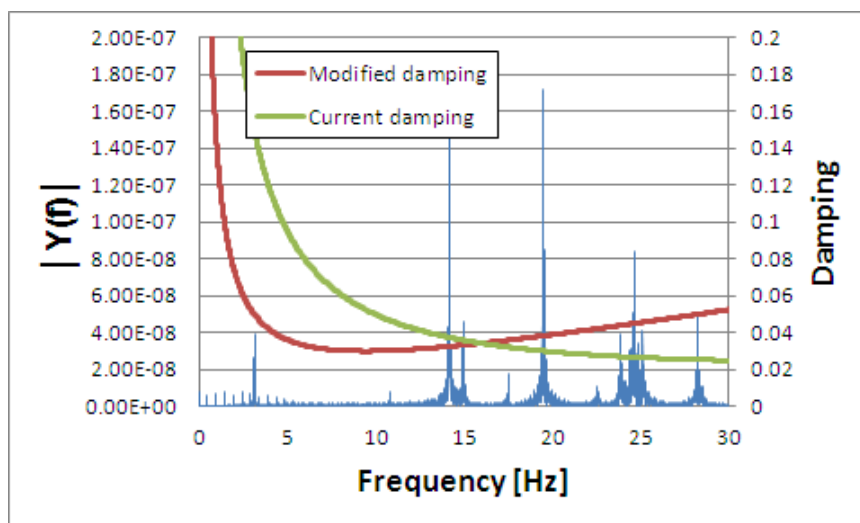


Figure 17. Fast Fourier transformation for the radial displacement data from node experiencing the maximum displacement during desynchronized loading and current and modified Rayleigh damping.



The time of occurrence of maximum von Mises stress in relation to the loading in case 1 and in case 2 (material damping included in both cases) is presented in Figure 18 and Figure 19, respectively. The time difference between the volume acceleration peak value and von Mises stress maximum for the synchronized loading is approximately 0,01s. The same time difference is drawn in Figure 19. The four last pipes in which chugging has occurred before the occurrence of the maximum von Mises stress, are 7, 16, 11 and 5.

In addition to the maximum value, the desynchronization also decreases the RMS values, due to the lower stress peaks. This is true also for the un-damped cases.

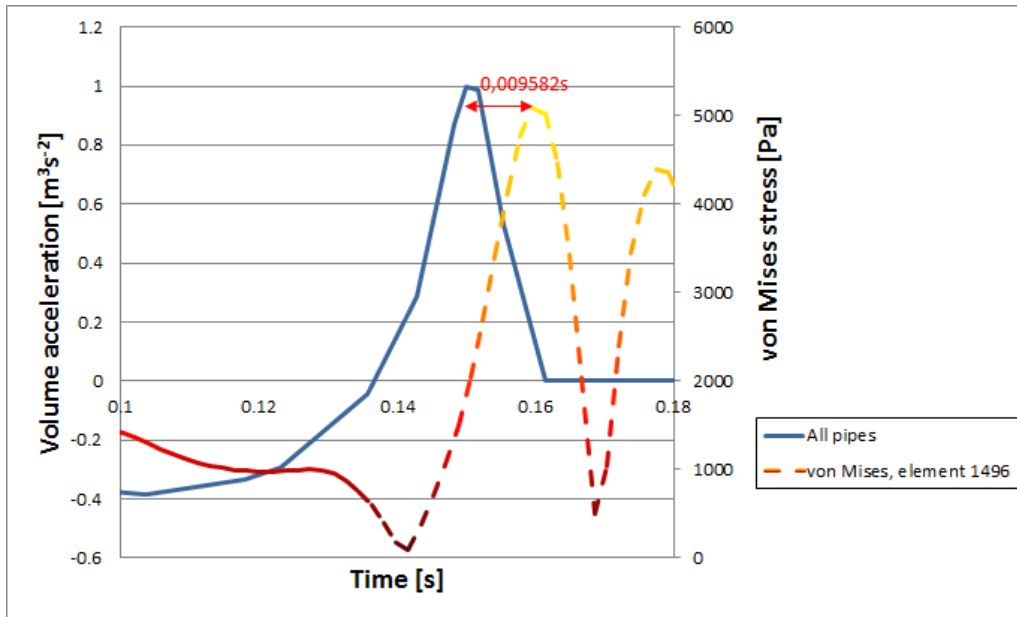


Figure 18. Loading at the time of occurrence of maximum von Mises stress in case of synchronized loading. The red line presents the von Mises stress in element 1496, in which the maximum value during the whole simulation occurred.

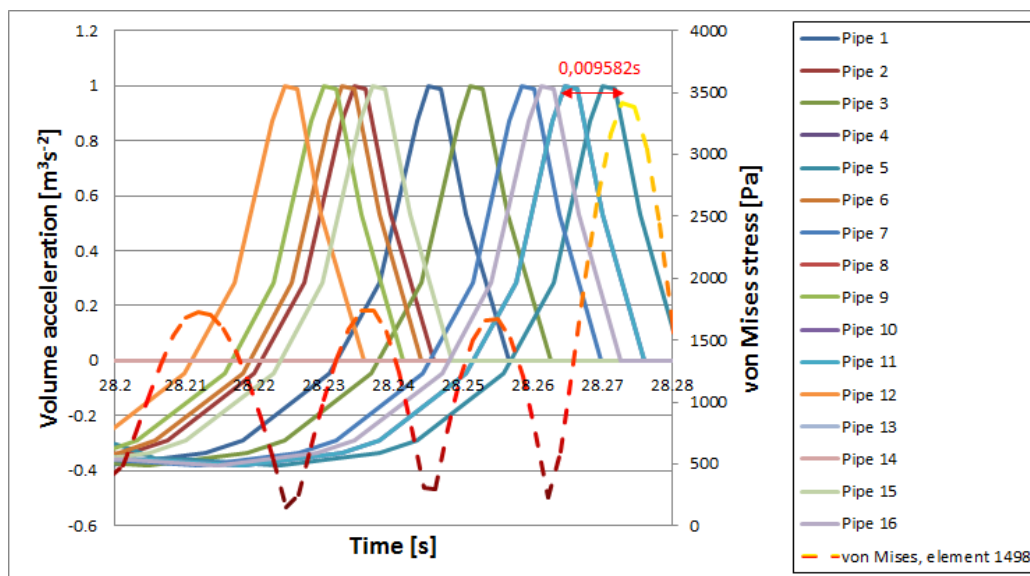


Figure 19. Loading at the time of occurrence of maximum von Mises stress in the case of desynchronized loading. The red line presents von Mises stress in element 1498, in which the maximum value during the whole simulation occurred. The last four pipes in which chugging has occurred are 7, 16, 11 and 5, so that pipe five is the last.

The location of the maximum von Mises stress varies around the inside surface of the outer wall of the containment, but the height in which the maximum stresses takes place, remains the same in all cases. The locations where the maximum stresses occur during synchronized and desynchronized loadings in the damped models are presented in Figure 20 and Figure 21, respectively. The von Mises stress as a function of time for the elements in which the maximum von Mises stress occurred in four different cases is presented in Figure 22(a)–Figure 22(d).

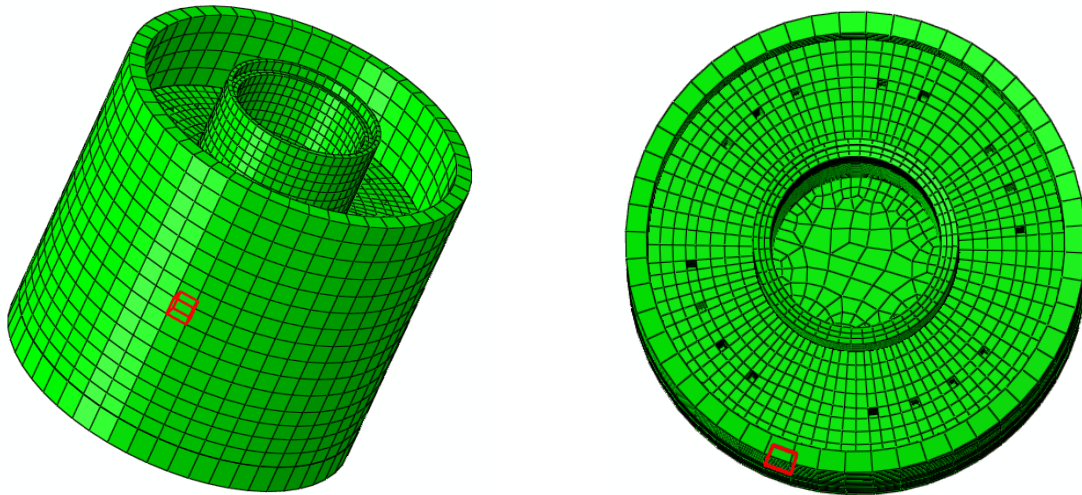


Figure 20. Location of element 1496, at which the maximum von Mises stress occurs in the synchronized case with material damping. The upper part of the containment is removed for better visualization of the location in relation to vent pipes.

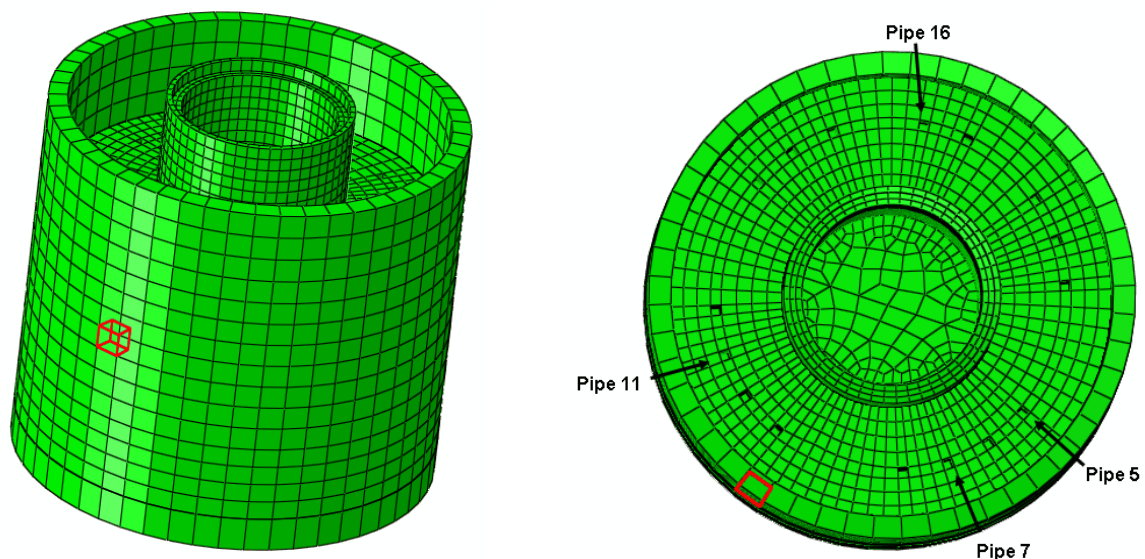


Figure 21. Location of element 1498, at which the maximum von Mises stress occurs in the desynchronized case with material damping. The upper part of the containment is removed for better visualization of the location in relation to vent pipes.



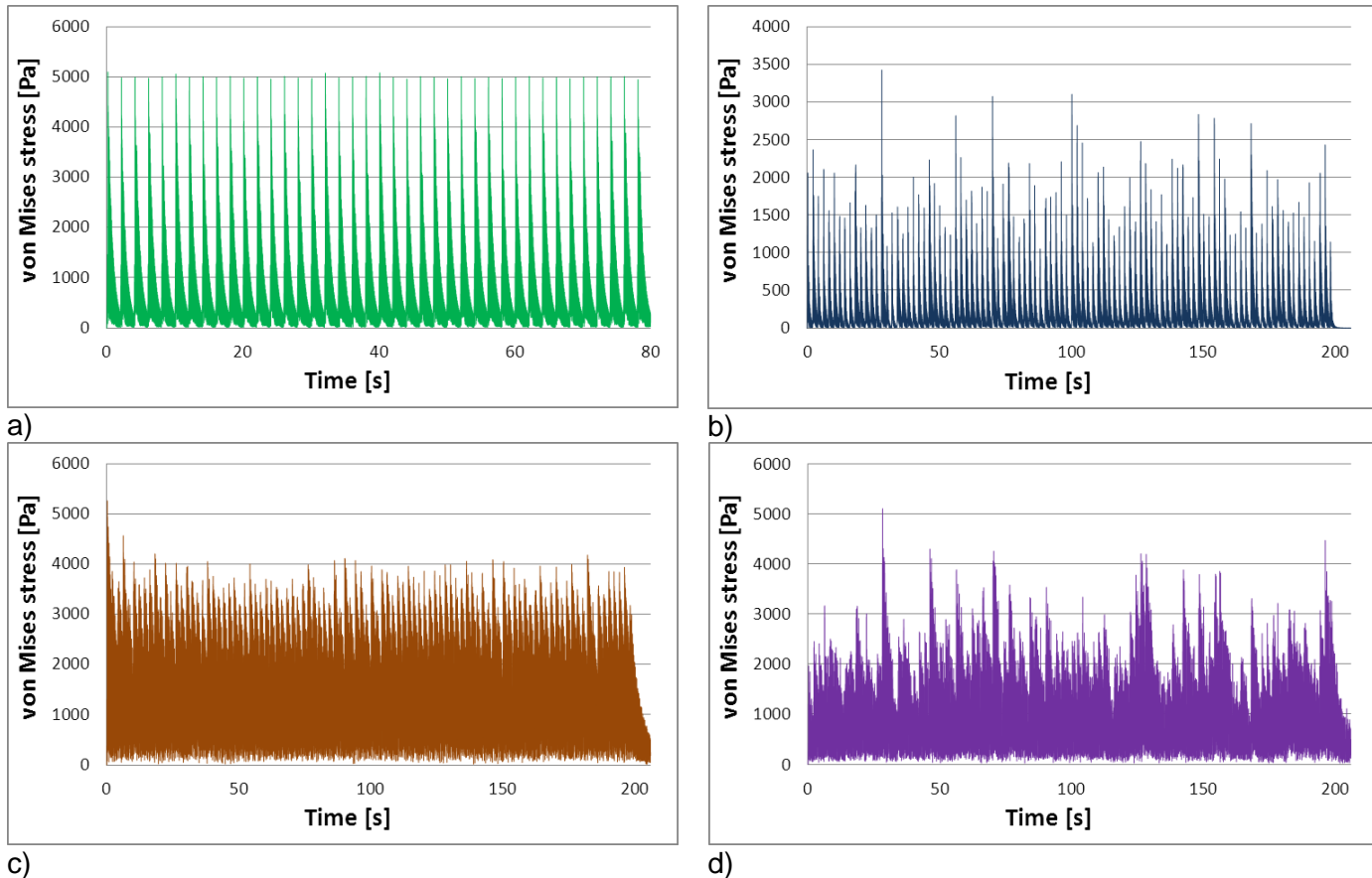
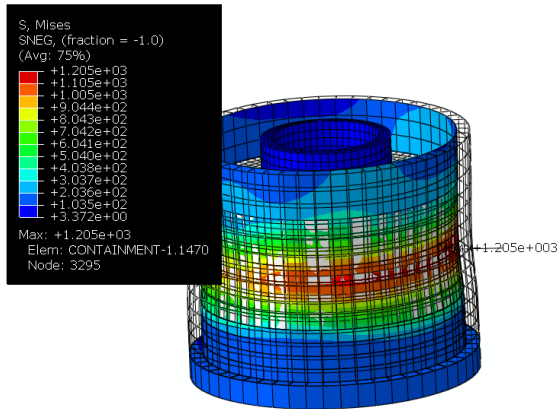


Figure 22. Von Mises stresses as a function of time at elements in which the maximums occur for a) synchronized loading with material damping, b) desynchronized loading with material damping, c) with synchronized loading, no material damping and d) desynchronized loading with no material damping.

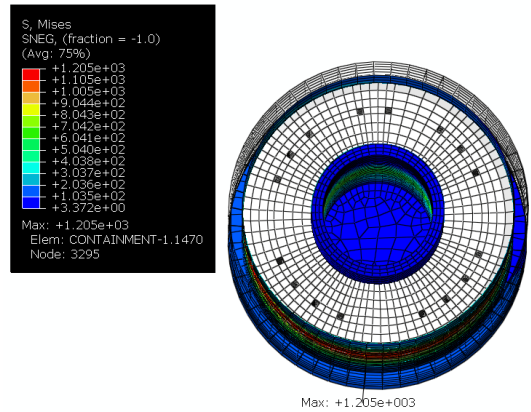
From the computed von Mises stresses, one can see that the response remains the same throughout the analysis during synchronized loading in the model where material damping is included, whereas in both cases where loading is desynchronized, the variance in the response is high, indicating high dependency on the desynchronization time. It can also be seen that even though the difference in the maximum von Mises stress is small between cases 3 and 4, in case 3 the containment repeatedly experiences high loads, whereas in case 4 the maximum is an individual peak value. This is also confirmed by the root mean squared von Mises value, which is significantly higher for case 3 (synchronized loading).

The maximum von Mises stresses and their location at different times during first chugging events for case 2 are presented in Figure 23. On the right hand side picture is shown the same instant of time as in the left hand side picture, but from above.



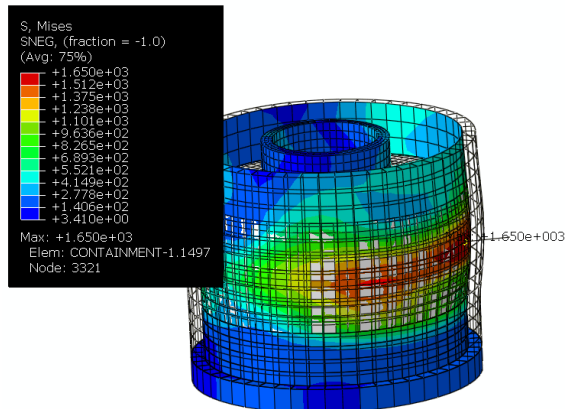
Step: Step-1  
 Increment: 12548; Step Time = 0.1800  
 Primary Var: S, Mises  
 Deformed Var: U; Deformation Scale Factor: +1.000e+06

a) von Mises stress at t=0.13s.



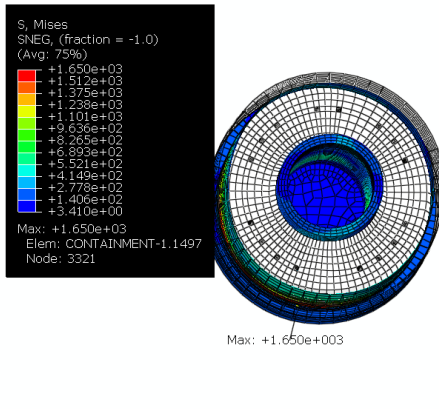
Step: Step-1  
 Increment: 12548; Step Time = 0.1800  
 Primary Var: S, Mises  
 Deformed Var: U; Deformation Scale Factor: +1.000e+06

b) von Mises stress at t=0.13s.



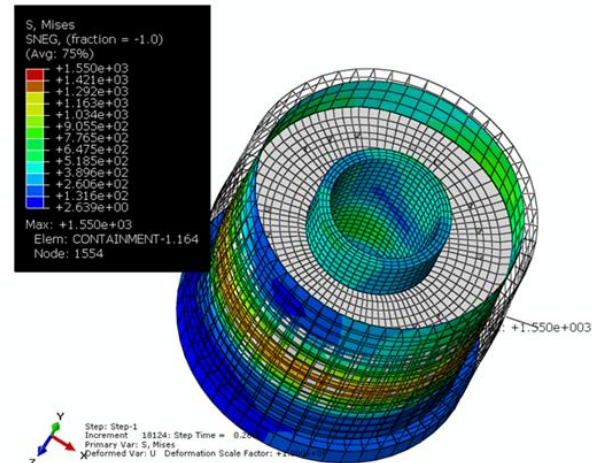
Step: Step-1  
 Increment: 16032; Step Time = 0.2300  
 Primary Var: S, Mises  
 Deformed Var: U; Deformation Scale Factor: +1.000e+06

c) von Mises stress at t=0.23s.



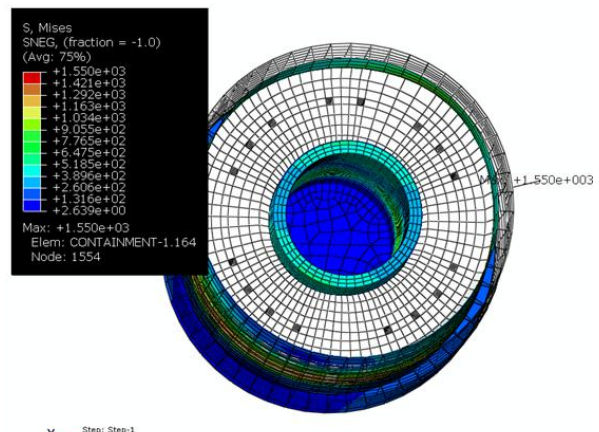
Step: Step-1  
 Increment: 16032; Step Time = 0.2300  
 Primary Var: S, Mises  
 Deformed Var: U; Deformation Scale Factor: +1.000e+06

d) von Mises stress at t=0.23s.



Step: Step-1  
 Increment: 18124; Step Time = 0.2600  
 Primary Var: S, Mises  
 Deformed Var: U; Deformation Scale Factor: +1.000e+06

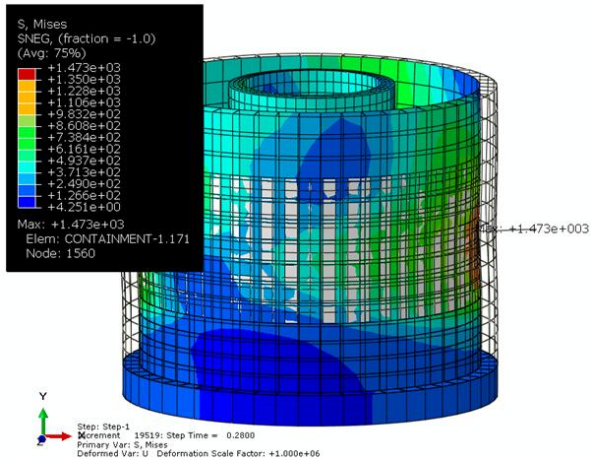
e) von Mises stress at t=0.26s.



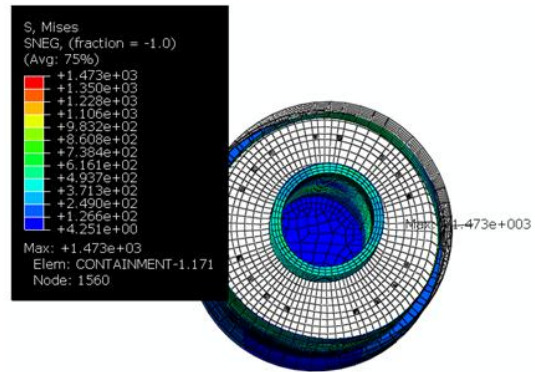
Step: Step-1  
 Increment: 18124; Step Time = 0.2600  
 Primary Var: S, Mises  
 Deformed Var: U; Deformation Scale Factor: +1.000e+06

f) von Mises stress at t=0.26s.

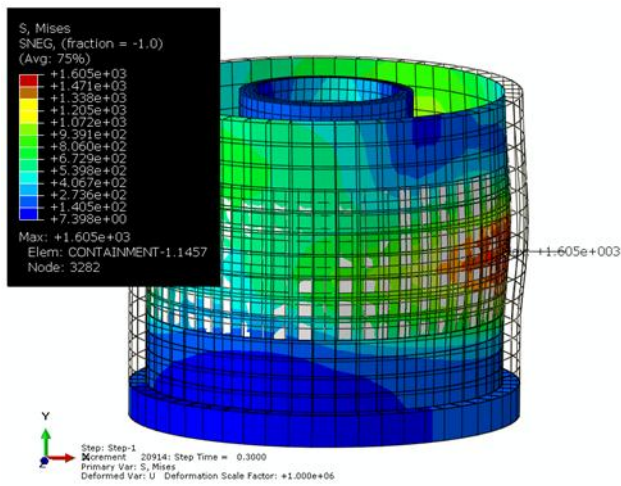
Figure 23. Maximum von Mises stress at different times. The pictures on the right-hand side present the deformation at the same time as the left-hand side picture, but from above.



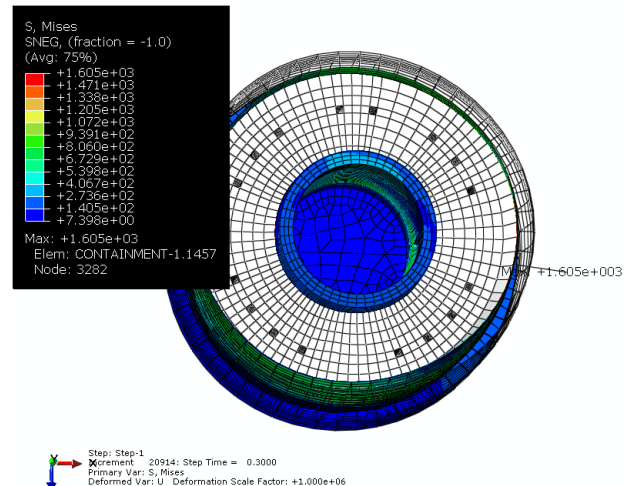
g) von Mises stress at t=0.28s.



h) von Mises stress at t=0.28s.



i) von Mises stress at t=0.3s.



j) von Mises stress at t=0.3s.

Figure 23. Continued from the previous page.

## 8. CFD modeling of PPOOLEX experiment MIX-03

---

The PPOOLEX experiment MIX-10 was used as a test case for the CFD model for direct-contact condensation. In the following, we first briefly describe the PPOOLEX facility and the experiment MIX-03. Then we present the results of the test simulation with the present version of the CFD model for direct-contact condensation.

### 8.1 PPOOLEX experiment MIX-03

The PPOOLEX facility is a pressurized cylindrical vessel with a height of 7.45 meters and a diameter of 2.4 meters. The volume of the drywell compartment is 13.3 m<sup>3</sup> and the volume of the wetwell compartment is 17.8 m<sup>3</sup>. Steam is blown into the drywell compartment via a horizontal DN200 inlet plenum. The experimental facility has earlier been described in detail by Puustinen, Laine and Räsänen (2010).

In 2012, MIX-03 experiment was performed, where stratification of the water pool was studied. In order to achieve stratification, a small flow rate of vapor was first injected through the drywell and vent pipe into the water pool. At a later stage, the flow rate of vapor was increased, so that mixing of the water pool was achieved. At this stage, chugging in the vent pipe started at time  $t = 2\,300$  s. In the following, we concentrate on this chugging stage of the experiment. Specifically, we study the phenomena at time  $t = 2\,600$  s, when the conditions were fairly stationary.

The CFD calculation was carefully initialized to correspond to the situation at time  $t = 2\,600$  s. It was assumed that the amount of non-condensable gas in the drywell was very small because almost all air had already been blown to the wetwell. The mole fraction of air in the drywell was assumed to be 0.01 %. The temperature of the gas in the drywell was 129 °C. Since the drywell was insulated, the walls were initialized to the same temperature. The pressure in the drywell was  $p_{DW} = 2.70$  bars. The temperature of the water pool was 27.5 °C, and the temperature of the gas space of the wetwell was about 50 °C.

The mass flow rate of vapor from the inlet plenum to the drywell was 0.432 kg/s and it was kept constant during the calculation. The temperature of the vapor was 142 °C and it contained a mass fraction of 0.01% of air.

### 8.2 Numerical model

The CFD calculations were performed by using the Euler-Euler two-phase model of ANSYS Fluent 14.5. The Euler-Euler model is a two-fluid model, where conservation of mass, momentum and energy are solved for gas and liquid water. The gas phase consisted of two species components: dry air and vapor.

The mass fraction of non-condensable gas flowing into the drywell was reduced from only 0.01 %. This means that in the drywell, the gas was almost pure vapor. The mixture of gases was modeled as an ideal gas. In the wall condensation and direct-contact condensation, the partial pressure model implemented earlier was applied, but some technical refinements that earlier limited the amount of direct-contact condensation were mitigated. The Hughes–Duffey model was used for heat transfer on the liquid side (Timperi et al., 2012).

In the spatial discretization, the QUICK scheme was used for all equations. The temporal discretization was first order. The turbulence was modeled with the standard  $k$ - $\varepsilon$  model for the mixture of the phases. The floating operating pressure option of Fluent was used for modeling the pressure increase in closed experimental facility.



### 8.3 Results of CFD simulations

The mass flow rate of vapor flowing into the vent pipe is illustrated in Figure 24. The clearing of the vent pipe occurs approximately at time  $t = 30$  s, and a large vapor bubble is formed at the vent outlet. The vent clearance is seen as a maximum in the mass flow rate in Figure 24. Another large bubble is formed and condensed about 0.7 s later. After this the water level stays close to the vent outlet but oscillates slightly with a period of about 0.2 s. One period of this rapid oscillation is illustrated in Figures 25–28.

In Figure 25, the void fraction near the vent outlet is shown. In the first frame, the mass flow rate of vapor into the vent pipe is small and all vapor is condensed at the outlet of the vent pipe. Later, the mass flow rate increases and a small toroidal bubble is formed around the outlet of the vent pipe. The bubble is condensed rapidly and the mass flow rate into the vent pipe decreases.

In Figure 26, the condensation rate of vapor is illustrated. In the first frame, the total direct-contact condensation rate is fairly small, i.e., 283 g/s. This is clearly smaller than the mass flow rate of vapor into the drywell, which is 432 g/s. Therefore, the pressure in the drywell increases slightly and a toroidal bubble is formed at the outlet of the vent pipe. When the surface area of the bubble increases, the total amount of condensation increases and has its maximum value of about 570 g/s at time interval 33.245...33.275 s. After this the bubble becomes smaller and the condensation rate decreases having the value 348 g/s in the last frame.

In the Hughes–Duffey model, the heat transfer coefficient on the liquid side of the interface of the phases is proportional to the square root of the turbulence kinetic energy. In Figure 27, the time evolution of the turbulence kinetic energy is shown. The maximum values of turbulence are about  $50 \text{ J/m}^3$ , and they are found slightly before the maximum condensation rate occurs.

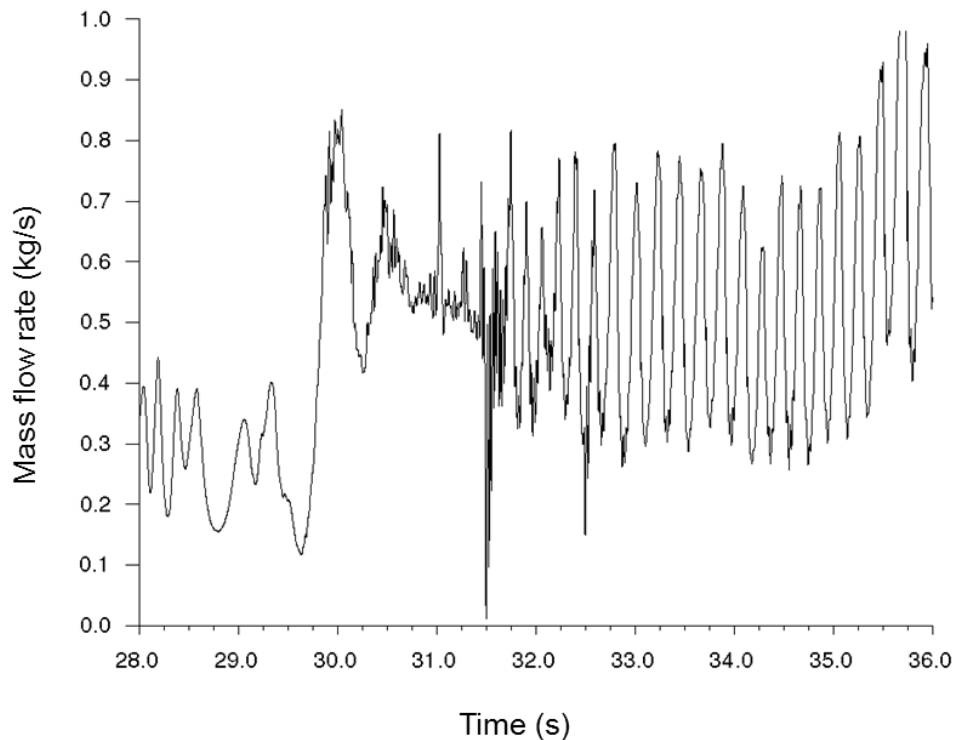


Figure 24. Mass flow rate flowing into the vent pipe.

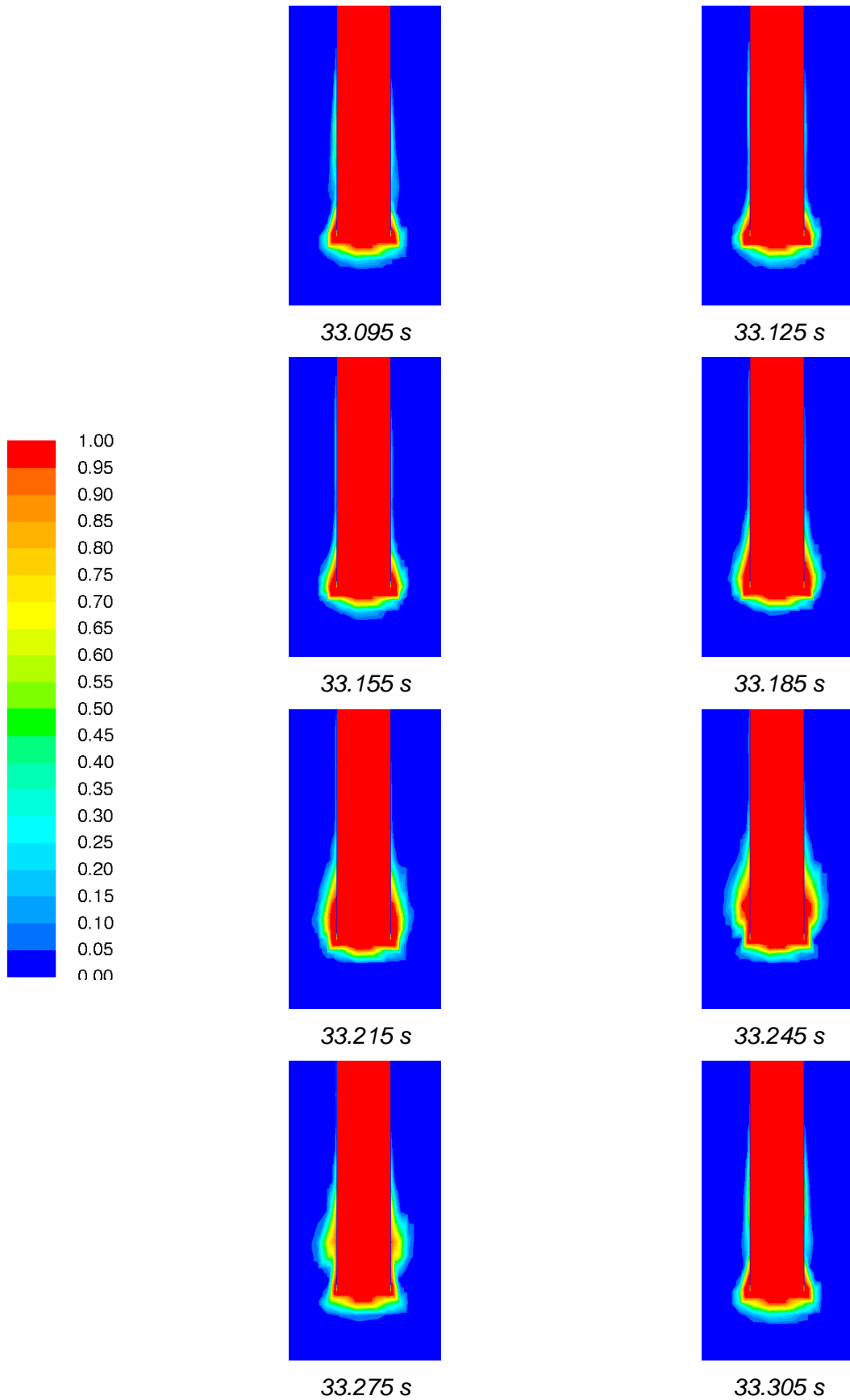


Figure 25. Volume fraction of gas at different instants of time during formation and condensation of a vapor bubble at the outlet of the vent pipe.

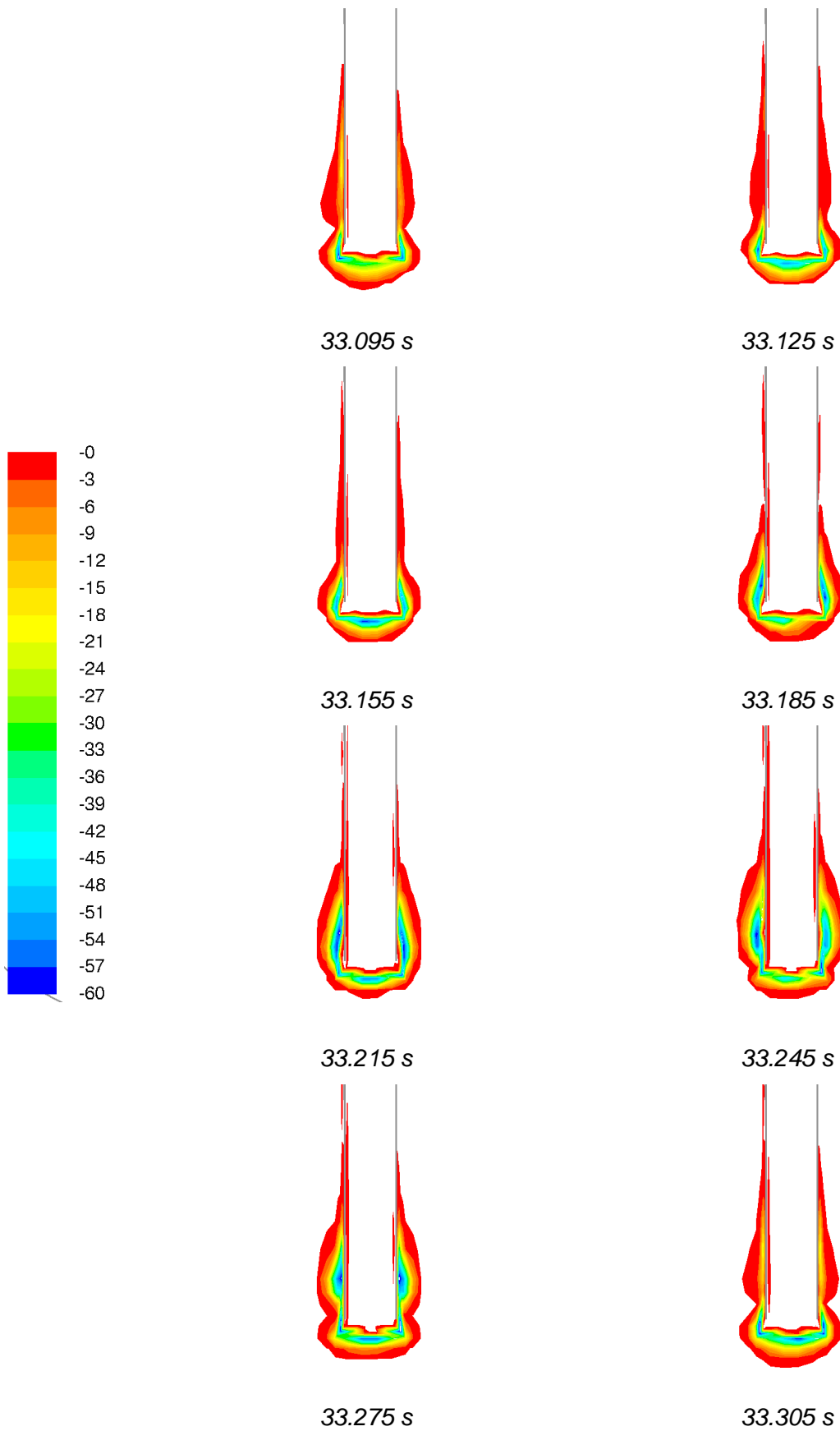


Figure 26. Condensation rate ( $\text{kg/m}^3\text{s}$ ) of vapor near the outlet of the vent pipe.

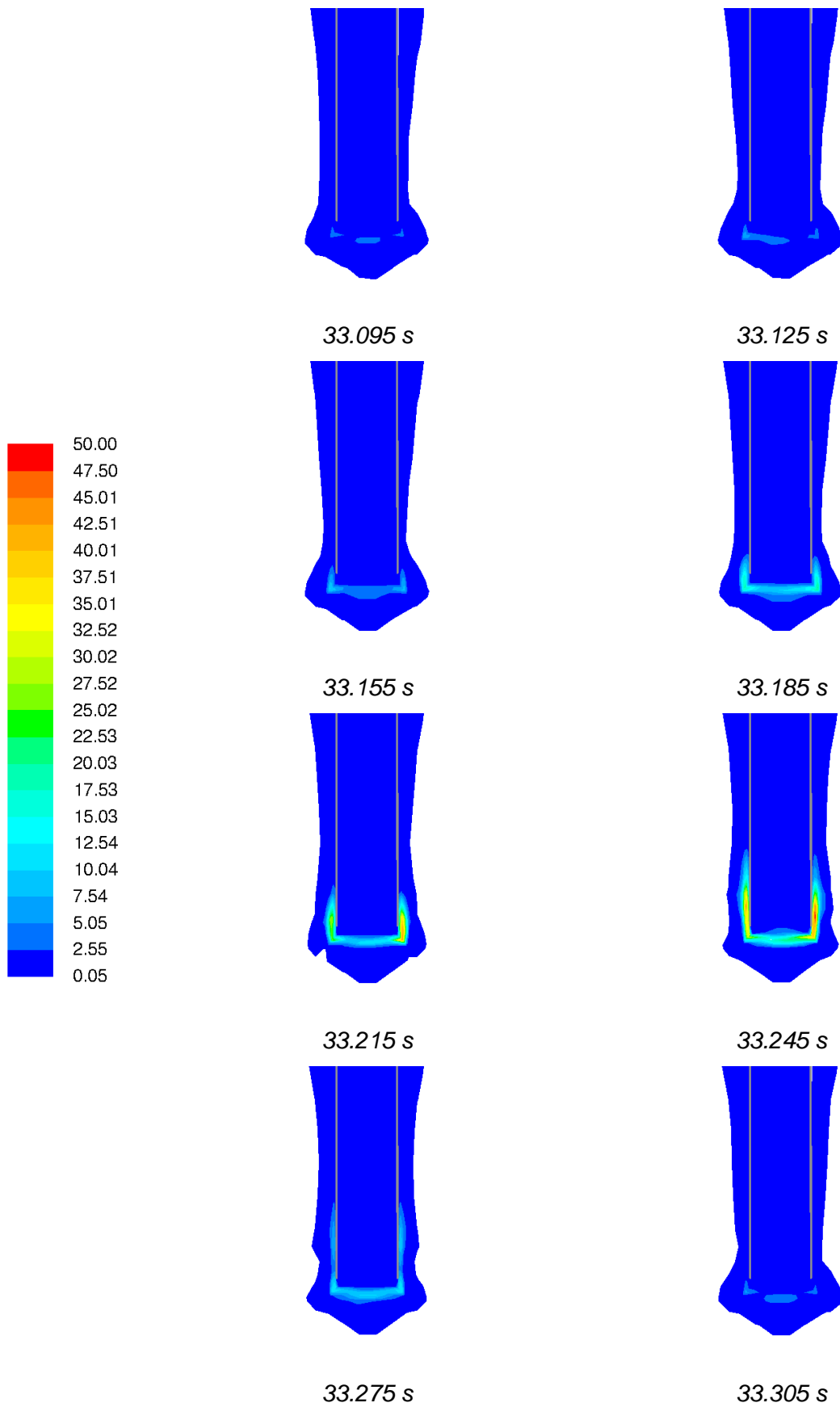


Figure 27. Turbulence kinetic energy ( $J/m^3$ ) near the outlet of the vent pipe. Note that the scale is logarithmic.



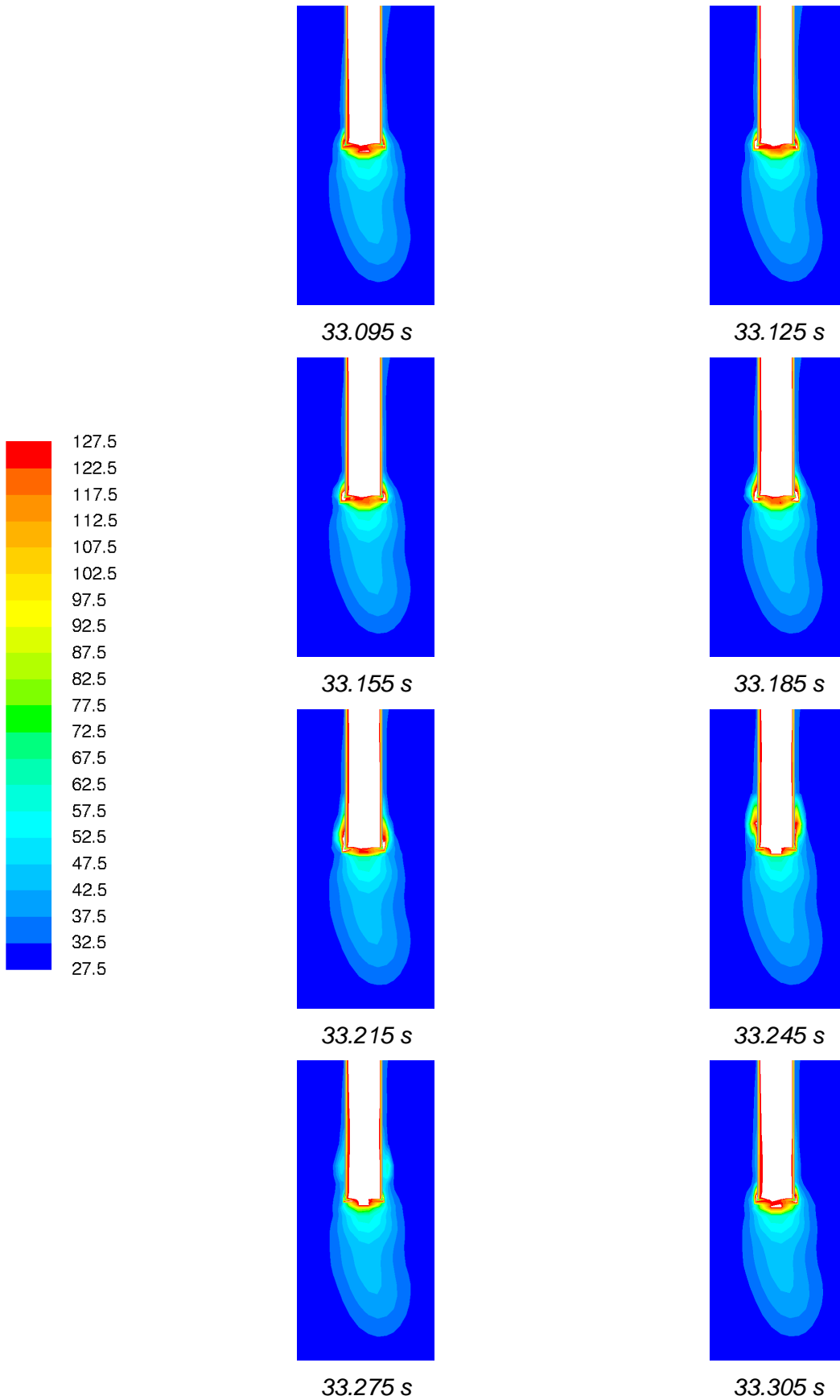


Figure 28. Liquid temperature (°C) near the outlet of the vent pipe.

In Figure 28, the liquid temperature near the vent outlet is shown. The temperature of saturated water is about 130 °C at the pressure of 2.70 bars. The hot vapor heats up the water near the vent outlet, and a fairly stable region of warm water is formed. Warming up of water decreases the condensation rate and stabilizes the flow of vapor.

In the experiment MIX-03, the chugging frequency was much smaller than the oscillation frequency in the present simulation. Typically, the chugging period was between 1.0...1.4 s compared to the oscillation period of the present calculation of 0.2 s. In general, the interphasial surface was too stable and remained persistently close to the outlet of the vent pipe. In the experiment, the longer chugging period was caused by the penetration of liquid water inside the vent pipe. There are several possible reasons for the difference. Note that a turbulence model for the mixture of the phases was used in the simulation. First, the turbulence model used in the simulation was for the mixture of the phases, but in the Hughes–Duffey correlation the turbulence kinetic energy for the liquid phase should be used. Second, the numerical mesh in the present simulation was fairly coarse, which increases numerical diffusion. A finer mesh will be tested in future.

## 9. Summary and conclusions

---

The rapid collapse of a large steam bubble was analyzed by using a 1D code which takes into account the finite condensation rate. The simulated results were compared with the PPOOLEX experiment COL-01. By adjusting the condensation rate, the calculated pressure peak near the vent outlet could be made same as in the experiment. This resulted in qualitatively correct behavior also for the low-pressure phase of the signal, although the calculated pressure drop was not as large as in the experiment. However, the calculated pressure peaks were sensitive to the condensation rate, making the simplified modeling assumptions questionable. When the condensation rate was set large enough to remove all or nearly all steam before the moment of peak volume acceleration, the pressure peaks became significantly too high. There are several possible reasons for the much lower and wider experimental pressure peaks compared to the calculations. Firstly, the condensation rate was constant in the calculations, but in reality the condensation rate may be large initially and slow down significantly, resulting in incomplete condensation in the final phase. Secondly, the real bubble shapes are fairly irregular and condensation may take place slightly “asynchronously” in different parts of the bubble. Thirdly, in the final phase the bubble shape may become highly irregular and/or the bubble surface may break into a “soft” two-phase mixture.

In the experiment COL-01 during the chugging phase, steam at the vent pipe outlet was only slightly superheated. As condensation occurs in the bubble, steam pressure in the bubble decreases rapidly. The present 1D calculations indicate that the pressure decrease is large enough to cause the steam to expand below the saturation line to a state of saturated mixture of steam and water mist (so-called wet steam).

Scaling of the measured pressure loads to full-scale was studied by dimensional analyses and by review of the Sonin (1981) analysis on SRV discharge. The main results of the Sonin (1981) analysis were that the pressure loads are same in the model and in the prototype, but the model time scales linearly with system size. The most important assumptions of the Sonin (1981) analysis were that the both systems are geometrically identical, operate at the same thermodynamic conditions and have same steam mass flux in the discharge pipe. Some of the assumptions made by Sonin (1981) are questionable for discharge through the open vent pipes during chugging, perhaps most importantly the assumption of negligible gravitational effects. In dimensional analysis of the bubble collapse, we found the same scaling properties as in the Sonin (1981) analysis and in the earlier numerical simulations (Timperi et al., 2012), namely that the pressure amplitude is independent of the system size

and that the bubble collapse time and pressure pulse duration scale linearly with the system size.

The structural response of containment during chugging was studied using a finite element model of containment with simplified geometry and loading which was created based on experimental data. The results were compared to a case in which desynchronization is absent, and chugging occurs simultaneous in every vent pipe. The desynchronized loading was created by giving random initiation times for chugs out of distribution corresponding to the desynchronization time presented by Kukita and Namatame (1985). Individual chug was modeled as volume acceleration, which represents the collapse of a steam bubble. The function of the volume acceleration was taken from a measured representative bubble collapse during single vent pipe test COL-01 (Timperi et al., 2012).

It was found that multiple chugging events could be simulated using explicit dynamics procedure, available in Abaqus. It was observed that desynchronization time in the loading decreases the maximum stresses significantly for the case where material damping was taken into account. In turn, the difference between the maximum stresses was very small between synchronized and desynchronized loading in cases where material damping was not considered. This resulted from the fact that the containment was still in motion caused by the previous group of chugs when next group of chugs took place. However, even though the difference in the maximum von Mises stress was small in the undamped cases between synchronized and desynchronized loading, in the case with synchronized loading, the containment repeatedly experiences high stresses, whereas in the desynchronized case, the maximum is an individual peak value, indicating that the loading is highly dependent on the desynchronization time.

In this study, the magnitude of the volume acceleration pulse was constant in every case and the speed of sound in the water was 1491 m/s. It is recommended that the variation in the volume acceleration of collapsing bubbles is added in the future analyses and the effect of speed of sound in the water during multiple chugging events is studied. Further, since the effect of the material damping was significant, it is recommended that the parameters of the Rayleigh damping are studied more closely and the sensitivity of the structural response to the variation in Rayleigh damping factors is investigated.

CFD simulations of the PPOOLEX experiment MIX-03 were performed. In the experiment, clear chugging behavior was observed. In the simulation, the interphasial surface was much more stable and oscillation occurred at a much higher frequency than in the experiment. The differences are likely caused by the turbulence model and too coarse numerical mesh, which causes numerical diffusion. Much improvement in the CFD model is still needed in order to produce reliable simulations of chugging.

## References

---

Abaqus, 2012. Analysis User's Manual, Dassault Systèmes, Providence, RI, Version 6.12-1.

Björndahl, O. and Andersson, M., 1998. Globala vibrationer vid kondensationsförlopp i wetwell orsakade av LOCA i BWR-anläggningar. Swedish Nuclear Power Inspectorate, SKI Report 99:3, Stockholm, 81 p.

Coste, P., 2013. A large interface model for two-phase CFD, Nuclear Engineering and Design **255**, pp. 38–50.

Ishii, M., Revankar, S.T., Leonardi, T., Dowlati, R., Bertodano, M.L., Babelli, I., Wang, W., Pokharna, H., Ransom, V.H., Viskanta, R. and Han, J.T., 1998. The three-level scaling approach with application to the Purdue University multi-dimensional integral test assembly (PUMA). Nuclear Engineering and Design, Vol. 186, pp. 177 - 211.

Kukita, Y. and Namatame, K., 1985. The vent-to-vent desynchronization effects on LOCA steam condensation loads in BWR pressure suppression pool. Nuclear Engineering and Design 85, pp. 141 - 150.

Laine, J., Puustinen, M. and Räsänen, A., 2009. PPOOLEX experiments with a modified blowdown pipe outlet. Lappeenranta University of Technology, Nuclear Safety Research Unit, Research report CONDEX 2/2008, 29 p. + app. 8 p.

Lahey, R.T., Jr. and Moody, F.J., 1993. The thermal-hydraulics of a boiling water nuclear reactor, 2nd edition, American Nuclear Society, USA.

Moody, F.J., 1990. Introduction to unsteady thermofluid mechanics, Wiley, New York.

Pankhurst, R.C., 1964. Dimensional analysis and scale factors. Chapman and Hall Limited, London.

Puustinen, M., 2006. Combined effects experiments with the condensation pool test facility. Lappeenranta University of Technology, Nuclear Safety Research Unit, Research report POOLEX 1/2006, 30 p. + app. 6 p.

Puustinen, M., Laine, J. and Räsänen, A., 2010. PPOOLEX experiments on dynamic loading with pressure feedback, Lappeenranta University of Technology, Nuclear Safety Research Unit, Research report CONDEX 2/2009, 42 p.

Puustinen, M., Laine, J. and Räsänen, A., 2011. Multiple blowdown pipe experiments with the PPOOLEX facility. Lappeenranta University of Technology, Nuclear Safety Research Unit, Research Report CONDEX 2/2010, 28 p. + app.8 p.

Pättikangas, T., Niemi, J. and Timperi, A., 2011. Numerical modelling of pressure suppression pools with CFD and FEM codes. VTT Technical Research Centre of Finland, Research Report VTT-R-00927-11, Espoo, Finland, 53 p.

Sonin, A.A., 1981. Scaling laws for small-scale modeling of steam relief into water pools. Nuclear Engineering and Design, Vol. 65, pp. 17 - 21.

Štrubelj, L. Ézsöl, G. and Tiselj, I., 2010. Direct contact condensation induced transition from stratified to slug flow, Nuclear Engineering and Design 240, 266 - 274.

Tanskanen, V., 2012. CFD modeling of direct contact condensation in suppression pools by applying condensation models of separated flow, *Acta Univesitatis Lappeenrantaensis* 472, Doctor's Thesis, Lappeenranta, Finland, 184 p.

Timperi, A., 2009. Fluid-structure interaction calculations using a linear perturbation method. 20<sup>th</sup> International Conference on Structural Mechanics in Reactor Technology, Espoo, Finland, August 9 - 14, 2009.

Timperi, A., Chauhan, M., Pättikangas, T. and Niemi, J., 2012. Modeling of interaction of multiple vent pipes in a pressure suppression pool. VTT Technical Research Centre of Finland, Research Report VTT-R-01094-12, Espoo, Finland, 54 p.

Wulff, W., 1996. Scaling of thermohydraulic systems. *Nuclear Engineering and Design*, Vol. 163, pp. 359 - 395.

Young, D.F., Munson, B.R. and Okiishi, T.H., 1997. *A brief introduction to fluid mechanics*. John Wiley & Sons, New York.

Title	Modelling of pressure loads in a pressure suppression pool
Author(s)	Antti Timperi, Michael Chauhan, Timo Pättikangas, and Jarto Niemi
Affiliation(s)	VTT Technical Research Centre of Finland
ISBN	978-87-7893-358-4
Date	June 2013
Project	NKS-R / ENPOOL
No. of pages	49
No. of tables	5
No. of illustrations	28
No. of references	20
Abstract	<p>Rapid collapse of a large steam bubble is analyzed by using CFD and FEM calculations. In addition, a 1D code is written which takes into account the finite condensation rate. The 1D simulations are compared with the PPOOLEX experiment COL-01. By adjusting the condensation rate, the calculated pressure peak near the vent outlet could be made same as in the experiment. Scaling of the measured pressure loads to full-scale is studied by dimensional analyses and by review of the analysis of Sonin (1981).</p> <p>The structural response of containment during chugging is studied by using an FEM of containment with simplified geometry and loading which was created based on experimental data. The results are compared to the case in which desynchronization is absent, and chugging occurs simultaneously in every vent pipe. The desynchronized loading is created by giving random initiation times for chugs out of distribution corresponding to the desynchronization time presented by Kukita and Namatame (1985).</p> <p>CFD simulations of the PPOOLEX experiment MIX-03 were performed. In the experiment, clear chugging behavior was observed. In the simulation, the interphasial surface was much more stable and oscillation occurred at a higher frequency than in the experiment. The differences are likely caused by the turbulence model and too coarse numerical mesh, which causes numerical diffusion.</p>
Key words	Condensation pool, pressure suppression pool, BWR, CFD, fluid-structure interaction, FSI, chugging, LOCA